REFERENCES AND NOTES

1. H. Matsushita *et al.*, *Nature* **482**, 400–404 (2012).
2. N. A. Rizvi *et al.*, *Science* **348**, 124–128 (2015).
3. J. C. Castle *et al.*, *Cancer Res.* **72**, 1081–1091 (2012).
4. A. Snyder *et al.*, *N. Engl. J. Med.* **371**, 2189–2199 (2014).
5. P. F. Robbins *et al.*, *Nat. Med.* **19**, 747–752 (2013).
6. T. N. Schumacher, R. D. Schreiber, *Science* **348**, 69–74 (2015).
7. M. Greaves, *Cancer Discovery* **5**, 806–820 (2015).
8. E. C. de Bruin *et al.*, *Science* **346**, 251–256 (2014).
9. M. Jamal-Hanjani *et al.*, *Ann. Oncol.* mdw037 (2016).
10. M. S. Lawrence *et al.*, *Nature* **505**, 495–501 (2014).
11. M. S. Rooney, S. A. Shukla, C. J. Wu, G. Getz, N. Hacohen, *Cell* **160**, 48–61 (2015).
12. S. A. Shukla *et al.*, *Nat. Biotechnol.* **33**, 1152–1158 (2015).
13. Materials and methods are available as supplementary materials on *Science* Online.
14. L. T. Nguyen, P. S. Ohashi, *Nat. Rev. Immunol.* **15**, 45–56 (2015).
15. S. R. Hadrup *et al.*, *Nat. Methods* **6**, 520–526 (2009).
16. S. Read, V. Malmström, F. Powrie, *J. Exp. Med.* **192**, 295–302 (2000).
17. E. M. Van Allen *et al.*, *Science* **350**, 207–211 (2015).
18. L. B. Alexandrov *et al.*, *Nature* **500**, 415–421 (2013).
19. B. E. Johnson *et al.*, *Science* **343**, 189–193 (2014).
20. T. A. Yap, M. Gerlinger, P. A. Futreal, L. Pusztai, C. Swanton, *Sci. Transl. Med.* **4**, 127ps10 (2012).
21. J. Zhang *et al.*, *Science* **346**, 256–259 (2014).

ACKNOWLEDGMENTS

C.S. is a senior Cancer Research UK (CRUK) clinical research fellow and is funded by CRUK (TRACERx), the CRUK Lung Cancer Centre of Excellence, Stand Up 2 Cancer Laura Ziskin prize (SU2C), the Rosetrees Trust, NovoNordisk Foundation (ID 16584), the Prostate Cancer Foundation, the Breast Cancer Research Foundation, the European Research Council (THESEUS), and EU FP7 (PREDICT). S.A.Q is funded by a CRUK Career Development Fellowship, CRUK Biotherapeutic Programme Grant, World Wide Cancer Research, and a Cancer Research Institute Investigator Award. A.J.S.F receives support from the Sam Keen Foundation. R.R., N.M., N.J.B., and G.A.W. are funded by the TRACERx CRUK grant. T.B.K.W. is funded by the FP7-People-2013-ITN [grant (2013)607722 – PloidyNet]. C.T.H. is funded by the Rosetrees Trust. C.J.W. is a Scholar of the Leukemia and Lymphoma Society and acknowledges support from the Blavatnik Family Foundation, NIH/National Heart, Lung, and Blood Institute (grant 1R01CA155010-02) and NIH/National Cancer Institute (grants 1R01CA182461-01 and 1R01CA184922-01). S.S. is funded by the Cancer Research UK–UCL Centre, and M.J.H. is funded by a CRUK-UCL Centre Clinical Research Fellowship. A.A. is funded by the Cancer Research UK–UCL Centre Cancer Immuno-Therapy Accelerator Award. We thank N. Hacohen and S. Turajlic for helpful advice on the manuscript. This research is supported by the National Institute for Health Research, the University College London Hospitals Biomedical Research Centre, and the Cancer Research UK University College London Experimental Cancer Medicine Centre. Certain data were received under a material transfer agreement with Memorial Sloan Kettering Cancer Center. Data from multiregion sequenced NSCLC are available at the European Bioinformatics Institute (accession no. EGAS00001000809). Data from the Rizvi cohort (*2*) are available at the database of Genotypes and Phenotypes (dbGAP) (accession no. phs000980.v1.p1). Data from the Snyder cohort (*4*) are available at dbGAP (accession no. phs001041.v1.p1). Data from the Van Allen cohort (*17*) are available at dbGAP (accession no. phs000452.v2.p1). The results published here are in part based on data generated by a TCGA pilot project established by the National Cancer Institute and National Human Genome Research Institute. The data were retrieved through dbGaP authorization (accession no. phs000178.v9.p8). Information about TCGA and the investigators and institutions that constitute the TCGA research network can be found at http://cancergenome.nih.gov. C.S. is a paid advisor for Janssen, Boerhinger Ingelheim, Ventana, Novartis, Roche, Sequenom, Natera, Grail, Apogen Biotechnologies, Epic Biosciences, and the Sarah Cannon Research Institute. D.S. is a paid advisor for Bristol-Myers Squibb, Roche, Novartis, Merck, and Amgen. B.S. is a paid advisor for Bristol-Myers Squibb. T.A.C. is a cofounder of and holds equity in Gritstone Oncology; is a paid advisor for Geneocea, OncoSpire, and Cancer Genetics; and receives funding from Bristol-Myers Squibb for research on the genomics of immune response. N.A.R. is a cofounder of and holds equity in Gritstone Oncology. E.M.V.A. is a paid advisor for Syapse, Roche Ventana, Takeda, and Third Rock Ventures. M.D.H is a paid advisor for Bristol-Myers Squibb, Merck, Genentech, AstraZeneca, and Neon. J.D.W is a paid advisor for Bristol-Myers Squibb. L.A.G. is a paid scientific advisor for Novartis, Boehringer Ingelheim, Foundation Medicine, and Warp Drive Bio. C.S., N.M., R.R., S.A.Q., and K.S.P. are co-inventors on UK patent applications (1516047.6, 1601098.5, 1601098.5, and 1601099.3) filed by Cancer Research Technology relating to methods for identifying and targeting neoantigens, methods of predicting prognosis of cancer patients, and/or identifying cancer patients who will benefit from treatment that involves determining the number of neoantigens.

SUPPLEMENTARY MATERIALS

www.sciencemag.org/content/351/6280/1463/suppl/DC1
Materials and Methods
Figs. S1 to S7
Tables S1 to S5
References (*22*–*38*)

15 August 2015; accepted 11 February 2016
Published online 3 March 2016
10.1126/science.aaf1490

TRANSPORTER FUNCTION

Direct observation of proton pumping by a eukaryotic P-type ATPase

Salome Veshaguri,[1,2,3,4] Sune M. Christensen,[1,2,3,4]* Gerdi C. Kemmer,[5] Garima Ghale,[1,2,3,4] Mads P. Møller,[1,2,3,4] Christina Lohr,[1,2,3,4] Andreas L. Christensen,[1,2,3,4] Bo H. Justesen,[5] Ida L. Jørgensen,[5] Jürgen Schiller,[6] Nikos S. Hatzakis,[1,2,3,4] Michael Grabe,[7] Thomas Günther Pomorski,[5] Dimitrios Stamou[1,2,3,4]†

In eukaryotes, P-type adenosine triphosphatases (ATPases) generate the plasma membrane potential and drive secondary transport systems; however, despite their importance, their regulation remains poorly understood. We monitored at the single-molecule level the activity of the prototypic proton-pumping P-type ATPase *Arabidopsis thaliana* isoform 2 (AHA2). Our measurements, combined with a physical nonequilibrium model of vesicle acidification, revealed that pumping is stochastically interrupted by long-lived (~100 seconds) inactive or leaky states. Allosteric regulation by pH gradients modulated the switch between these states but not the pumping or leakage rates. The autoinhibitory regulatory domain of AHA2 reduced the intrinsic pumping rates but increased the dwell time in the active pumping state. We anticipate that similar functional dynamics underlie the operation and regulation of many other active transporters.

Electrochemical gradients across cellular membranes control many essential biological processes. These gradients are generated by primary active transporters and are used to drive the exchange of other solutes through secondary active transporters and to facilitate signaling through ion channels (*1*). Patch clamp recording has made it possible to observe the functional dynamics of single ion channels, revealing discrete on and off states, subconductance states, and other mechanistically important features that macroscopic experiments cannot probe (*2*). However, despite extensive structural and biochemical efforts (*3*), we currently lack a similar depth of understanding of transporters, because they in general do not produce electrically detectable single-molecule transport signals (*4*–*8*). We monitored at the single-molecule level the functional dynamics of a eukaryotic primary active transporter, *Arabidopsis thaliana* H^+–adenosine triphosphatase (ATPase) isoform 2 (AHA2, referred to as the proton pump), which is responsible for energizing the plasma membrane of plants and fungi (figs. S1 and S2) (*3*, *9*). This provided insights into how the activity of P-type ATPases is modulated by autoregulatory terminal domains (R domains) and pH gradients (*10*, *11*).

We used total internal reflection fluorescence (TIRF) microscopy to image with high throughput single nanoscopic lipid vesicles tethered to a solid support (Fig. 1, A and B, and figs. S3 and S4). Tethering was accomplished with a biotin/neutravidin protocol (*12*), which maintains the native function and diffusivity of reconstituted transmembrane proteins (*13*) and the vesicles' spherical morphology (*14*) and low passive ion permeability (*15*). The fluorescence intensity of all single vesicles was quantitatively converted to pH (fig. S5) and tracked over periods of up to 30 min.

Initial studies were carried out on the well-studied activated form of AHA2, which lacks the

[1]Bionanotecnology and Nanomedicine Laboratory, University of Copenhagen, Copenhagen, Denmark. [2]Department of Chemistry, University of Copenhagen, Copenhagen, Denmark. [3]Nano-Science Center, University of Copenhagen, Copenhagen, Denmark. [4]Lundbeck Foundation Center Biomembranes in Nanomedicine, University of Copenhagen, Copenhagen, Denmark. [5]Centre for Membrane Pumps in Cells and Disease - PUMPKIN, Department of Plant and Environmental Sciences, University of Copenhagen, Frederiksberg, Denmark. [6]Institute of Medical Physics and Biophysics, Faculty of Medicine, University of Leipzig, Leipzig, Germany. [7]Cardiovascular Research Institute, Department of Pharmaceutical Chemistry, University of California, San Francisco, CA 94143, USA.
*Present address: Novozymes A/S, 2880 Bagsvaerd, Denmark.
†Corresponding author. E-mail: stamou@nano.ku.dk

flexible C-terminal autoinhibitory R domain ($AHA2^R$) (Fig. 1A and figs. S1 to S3) (*9*). Initialization of H^+ pumping into the vesicle lumen was triggered by the addition of ATP and Mg^{2+}, which are non–membrane-permeable and thus only activate proton pumps with an outward-facing ATP-binding domain (Fig. 1A) (*12*). Consistent with this, we never observed lumenal alkalinization (Fig. 1C). Acidification kinetics reached a plateau of well-defined pH (ΔpH_{max}) as a result of a dynamic steady state, in which active pumping (influx) of protons matched the passive leakage (efflux) of protons through the membrane due to the buildup of a proton motive force (*16*). As expected, addition of the protonophore CCCP collapsed the H^+ gradients (Fig. 1C), whereas controls performed without Mg^{2+}, ATP, or $AHA2^R$ showed no response (fig. S6D). Furthermore, the activity of the pump was blocked by the addition of the specific inhibitor vanadate (*11*), and it decayed after ATP and Mg^{2+} were flushed out (fig. S7). To control for potential artifacts arising from the surface tethering of vesicles, we performed a side-by-side comparison with vesicles suspended in solution, which proved indistinguishable within experimental uncertainties (Fig. 1C and fig. S6). Taken together, these results demonstrate that we were able to observe the $AHA2^R$-mediated and ATP-fueled pumping of protons against their concentration gradient into the lumen of single vesicles. The single-vesicle experiments revealed a heterogeneity of acidification rates and ΔpH_{max} values between vesicles (Fig. 1C) that remain masked in the ensemble averages (*16*).

At the low protein-to-lipid molar ratio (1:12,000) used in our experiments, 84% of vesicles exhibited no detectable pH changes (Fig. 1C and Fig. 2A, top trace) indicating the absence of active pumps and thus suggesting that there are only a few active pumps in each of the remaining vesicles whose pH changed over time (hereafter termed active vesicles). We inspected the pH changes in the 16% of active vesicles and indeed found that all of them exhibited the hallmark of single-molecule behavior; i.e., stochastic changes between discrete states (Fig. 2A). Because the passive leakage rates of the vesicles are constant over time (fig. S10), these data demonstrate that the individual proton pumps are stochastically transitioning between active and inactive states. This behavior is termed functional dynamics (*17*–*24*) and is key to the function and regulation of ion channels (*25*).

Further examination of all active vesicle traces revealed that ~60% of them reverted back to the zero ΔpH baseline after switching off, strongly suggesting the presence of only one molecule, because it is improbable for many molecules to switch off simultaneously (Fig. 2A). In the remaining traces (~40%), we observed two or three discrete plateaus, a feature that has been observed in all studies of single channels to date and has been interpreted to demonstrate that the activity of multiple single molecules can be discretely resolved. The latter conclusion was further supported by experiments in which titration of the protein–to-lipid ratio modulated the percentage of multiple plateaus (fig. S5G), excluding the possibility that multiple plateaus represent multiple single-molecule activity states. These observations allowed us to unambiguously identify the traces resulting from a single active proton pump, which we then selected for further analysis. The activity of single proton pumps was amplified and reported by ~10^3 pH-sensitive fluorophores (figs. S3 and S4) (*16*), circumventing the issue of photobleaching that fundamentally restricts most fluorescence studies of single molecules.

Dynamic transitions between active and inactive states were also observed in experiments with wild-type AHA2 (Fig. 2C), demonstrating that they are not solely a property of the truncated version. Here ~80% of all vesicles were inactive, whereas ~73% of those that showed activity had a single plateau indicating a single molecule (Fig. 2D). With wild-type AHA2, we succeeded in using a SNAP-tag to fluorescently label the protein and count directly the number of proteins per vesicle (Fig. 2E). This allowed us to observe activity dynamics and directly count the number of labeled proteins at the same time on the same vesicles (Fig. 2C and 2E). We then estimated the labeling efficiency and the probability that a proton pump was active (*12*). We were thus able to quantitatively convert the bleach-step distribution to a distribution of active molecules per vesicle and demonstrated that 70 ± 15% of active proteoliposomes carried one active molecule (Fig. 2F). This was in quantitative agreement with the distribution of activity plateaus (~73%) (Fig. 2D), providing an additional demonstration that we can resolve and record the functional dynamics of the proton pump at the single-molecule level.

The activity of the proton pump, and probably other active transporters, is thus not constant in time (Fig. 2). Therefore, for transporters (just like ion channels), the rates measured in macroscopic experiments are the product of the active-state probability and the intrinsic pumping rate. To quantitatively analyze the kinetics and dynamics of pumping, we constructed a physical model of a single vesicle (*12*), which accounts for several parameters that affect the acidification kinetics, including passive and active ionic fluxes across

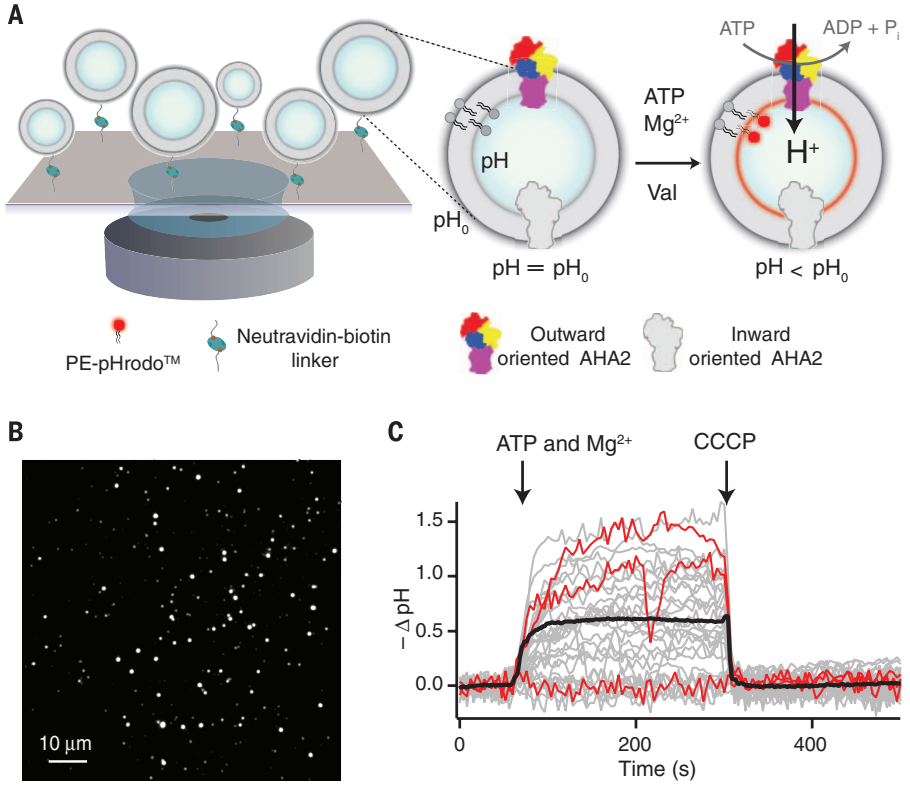

Fig. 1. Imaging proton pumping into the lumen of single surface-tethered vesicles using TIRF microscopy. (**A**) Illustration of AHA2 reconstituted vesicles tethered to a passivated glass surface and imaged on and individual basis with TIRF microscopy. Zoom: Extravesicular addition of both ATP and Mg^{2+} activated exclusively outward-facing AHA2 molecules, triggering H^+ pumping in the vesicle lumen. We quantified changes in the vesicular H^+ concentration by calibrating the response of the lipid-conjugated pH-sensitive fluorophore pHrodo. Valinomycin was always present to mediate K^+/H^+ exchange and prevent the buildup of a transmembrane electrical potential. (**B**) TIRF image of single vesicles tethered on a passivated glass slide. (**C**) Acidification kinetics of single vesicles upon addition of ATP and Mg^{2+}. Red traces highlight three representative signals from single vesicles, showcasing the absence of transport activity, the continuous pumping of protons, and fluctuations in proton-transport activity. The black trace is the average of ≈600 single-vesicle traces. As expected, addition of the protonophore CCCP collapsed the proton gradient established by $AHA2^R$.

the membrane, proton buffering in the lumen, vesicle size, and buildup of membrane potential (Fig. 3A) (*26*). Proton pumping is modeled with a fixed rate (I_P), a lifetime (t_{on}), and time between pumping events (t_{off}) Fig. 3, A and B. The vesicle is assumed to have a passive membrane permeability to protons (P_{leak}), which is constant over time, as revealed by control experiments (fig. S10). The stochastic switching of the pump between active and inactive states was extracted directly from the traces and used as time-dependent input to the model. The model is constrained to fit the entire trace, and it provides a realistic description of the full electrochemical gradient and a direct estimation of the absolute numbers of pumped and leaked ions.

Initially, all experimental traces were fit with the model by varying two parameters: I_P and P_{leak}. This provided a good quantitative description of the majority of AHA2^R traces (~65% of 126 counts, fig. S8); however, it systematically underestimated the observed leaking rates for the remaining traces (Fig. 3B, blue line), suggesting the existence of an additional proton-leaking route apart from passive leakage through the membrane (fig. S8). Indeed, leakage of ions through transporters has been reported before; e.g., for P- and V-type ATPases (*27*, *28*). To test this hypothesis, we collected all lifetimes of exponential fits to the leakage kinetics from traces transitioning between active and inactive states. The histogram of leakage lifetimes (fig. S9C) had two clearly separated peaks: one that according to control experiments corresponded to passive leakage through the membrane (a transmembrane leak) and another that was approximately 20 times faster (figs. S9 and S10). The latter peak was specifically inhibited by the addition of vanadate, which locked the pump in the E2 state (*11*) (fig. S9D), demonstrating that the leak is not passively mediated by the membrane (or the protein/membrane interface) but by the pump itself. Because vanadate is membrane-impermeable, we can exclude the possibility that the fast-leak component originated from pumps with the opposite orientation, because they would not be blocked by vanadate. We thus modified the model to include a time-dependent transprotein proton leak (P_{AHA2}), which turns on once pumping stops and turns off at the beginning of the next pumping cycle (Fig. 3C, blue dotted line). As expected, the revised model considerably improved the fits of the remaining traces (Fig. 3B, red line, and fig. S8).

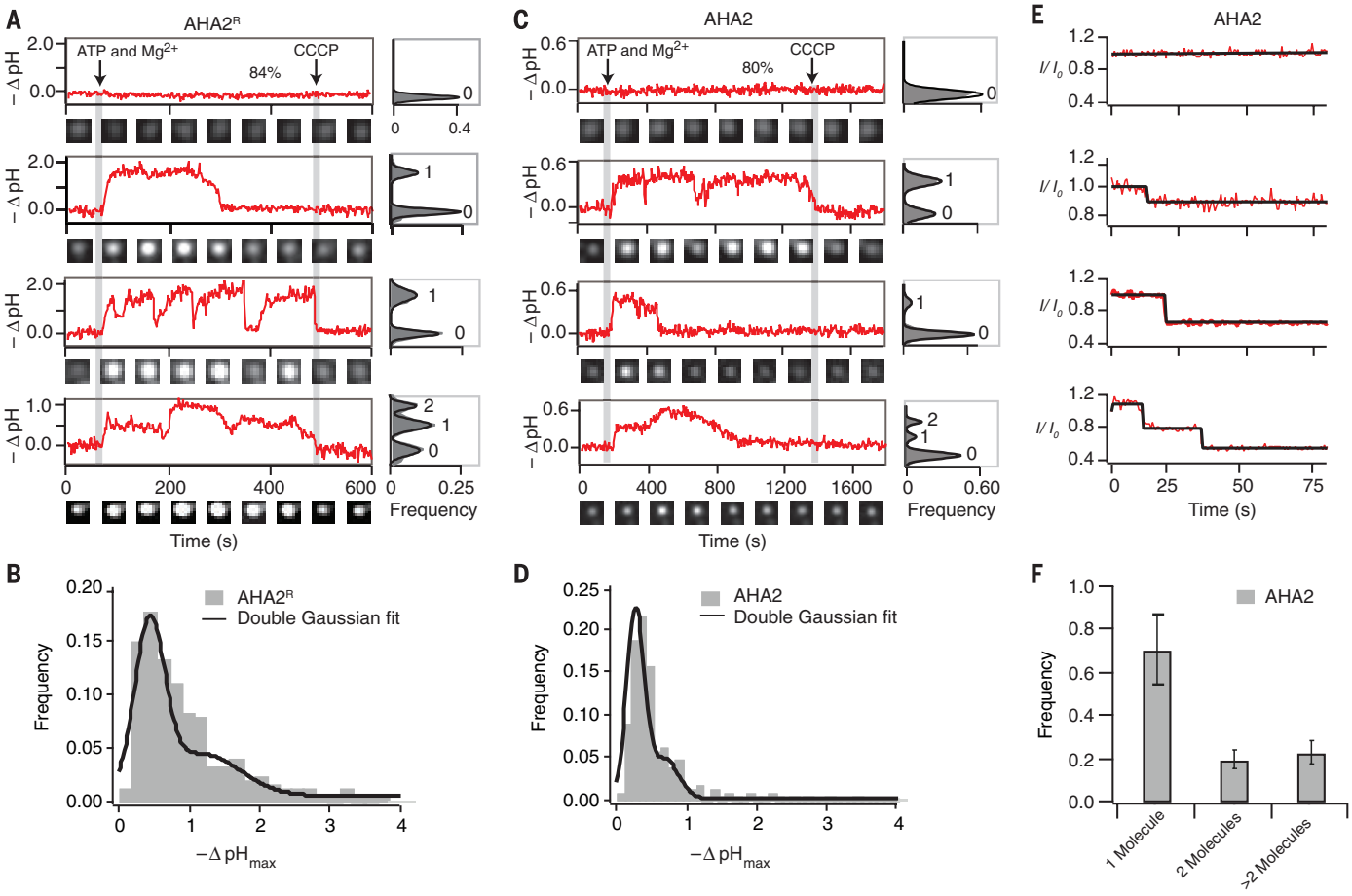

Fig. 2. Single-molecule observation of proton pumping reveals active and inactive states. (**A**) Typical examples of pH changes inside individual AHA2^R reconstituted vesicles. ATP and Mg^{2+} (2 mM) were added to initiate proton pumping, and CCCP (5 μM) was added to collapse the pH gradients. Traces show −ΔpH defined as a difference between the initial and final pH. Images of each respective liposome at different time points are shown below each trace. At the right-hand side of the traces, we plotted histograms of pH plateaus numbered to indicate the number of active pumps per vesicle. The pH inside the majority of vesicles showed no changes indicating the absence of functional transporter molecules (top panel). For the majority of active vesicles, we observed intermittent H^+ pumping, indicating the presence of single molecules (middle panels). The observation of two discrete steady-state pH plateaus in single-vesicle traces indicated the occasional presence of two active pumps per single vesicle (bottom panel). (**B**) Population histogram of pH plateaus for AHA2^R-reconstituted vesicles (n = 3, where hereafter n is the number of independent experiments). (**C** and **D**) Same as in (A) and (B) but for full-length AHA2. For (D), n = 2. Labeling of AHA2 with Alexa Fluor 647 enabled counting on the same vesicles of both the number of labeled AHA2 proteins (**E**) and of the respective activity dynamics (C). (**F**) The histogram of active proteins per vesicle was calculated from step-bleaching analysis of the data in (E) that was corrected for labeling efficiency and the probability that a proton pump is active (*12*). The two independent methods for estimating the number of active molecules agreed that ~70% of vesicles containing a protein have one active proton pump.

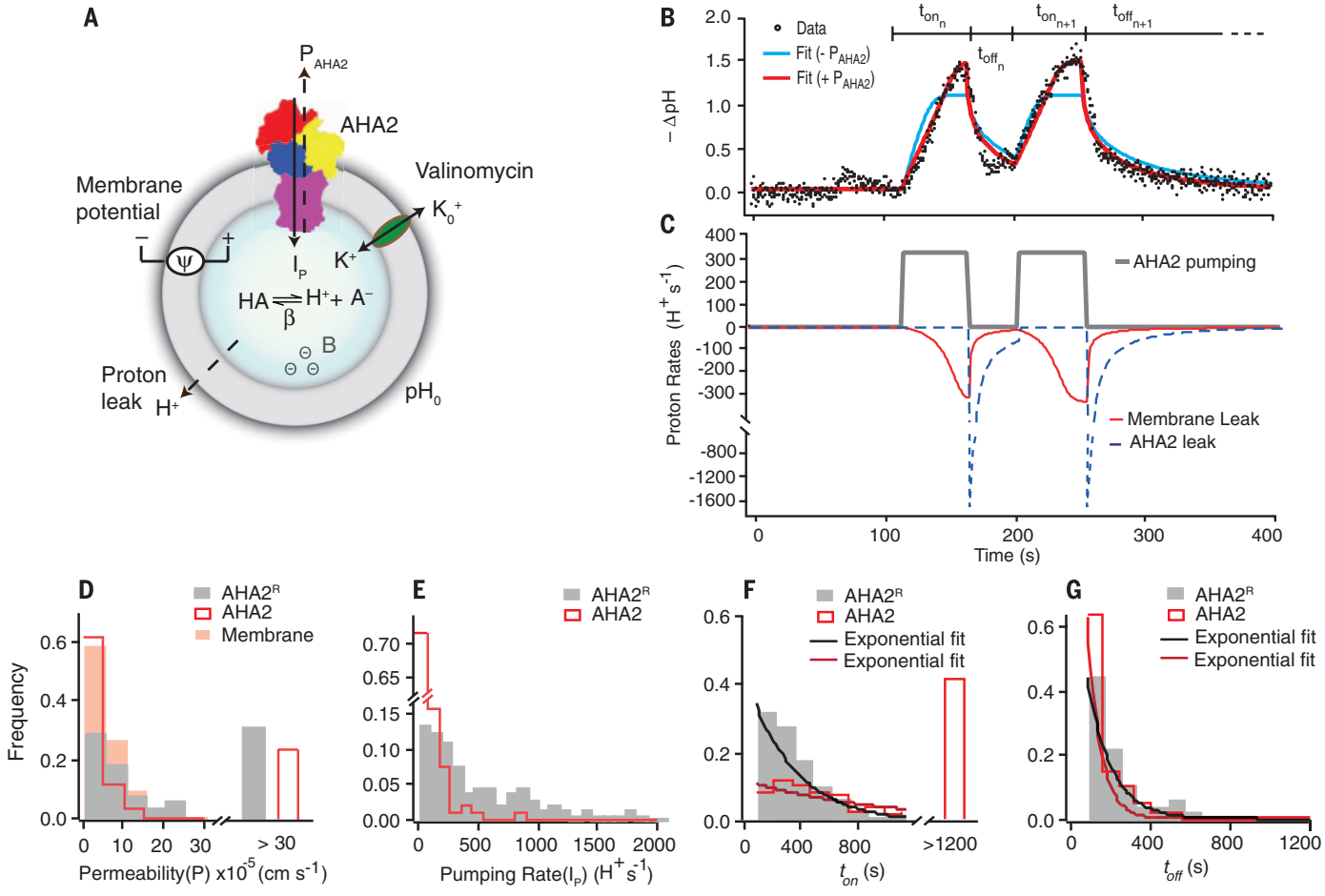

Fig. 3. Modeling active, inactive, and leaky states and their role in auto-inhibiting proton pumps. (**A**) The main parameters of the physical model we used to fit changes in the vesicular pH were pumping rate (I_p), protein-associated leak (P_{AHA2}), membrane leak (P_{leak}), valinomycin-induced K^+ permeability (P_{K+}), buffering capacity in the interior of the vesicle (β), and electrical potential across the membrane (Ψ) (*12*). (**B**) Example of a typical proton pumping trace and respective fits without (blue) and with (red) a transprotein proton leak. A threshold in the first derivative of the pH kinetics (*12*) was used to define the lifetime of the active state t_{on} and the time between pumping events t_{off}. (**C**) Temporal evolution of the proton pumping rate (gray) and the proton efflux rates due to passive membrane (red) leakage and transprotein backflow (blue) for the pH trace shown in (B). (**D**) Histogram of proton permeability associated with the membrane, AHA2, and AHA2^R. Respective counts were 95, 37, and 45. (**E**) Histogram of pumping rates for AHA2^R and AHA2. Respective counts were 126 and 95. (**F**) Histogram of t_{on} for AHA2^R and AHA2. Respective counts were 241 and 134. The bar at >1200 s shows the number of traces that did not switch in the duration of the experiment. (**G**) Histogram of t_{off} for AHA2^R and AHA2. Respective counts were 69 and 39. For AHA2^R and AHA2, respectively, the number of independent experiments was 3 and 2 and the number of individual proteoliposomes analyzed was 126 and 95.

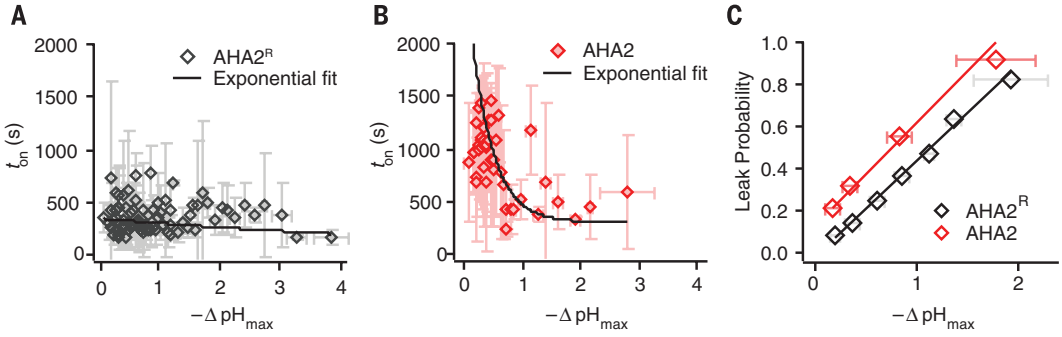

Fig. 4. Regulation of proton pumping by pH gradients. (**A** and **B**) Relation between t_{on} and the maximal pH gradient for AHA2^R and AHA2, respectively. Each data point represents the average of three consecutive values. Error bars represent corresponding standard deviations. The decay constants from the error-weighted exponential fits to the data are 6.9 ± 2.0 s and 0.4 ± 0.1 s for (A) and (B), respectively, where uncertainties represent 95% confidence intervals from the fits. (**C**) Probability of observing a transprotein leak as a function of pH gradient. For AHA2^R and AHA2, data were binned with 0.25 and 0.5 pH units; the number of independent experiments and individual proteoliposomes analyzed was the same as in Fig. 3. Spearman's rank order correlation coefficients ρ (126) = 0.40, $P = 10^{-4}$, and ρ (95) = 0.30, P = 0.03 indicated a strong positive correlation between leakage probability and ΔpH_{max} for both AHA2^R and AHA2.

Next, we quantitated proton permeabilities by fitting the kinetics with the model. The average transmembrane leak P_{leak} (Fig. 3D and fig. S11) was ~7×10^{-5} cm/s, which is in line with previous measurements and estimates (*26*), and the average transprotein leak P_{AHA2} had a similar value (~46×10^{-5} cm/s) (Fig. 3D). However, when normalized for surface area, the transprotein proton current was greater than the transmembrane by a factor of ~10^4.

The inhibitory R domain of AHA2 has been shown to reduce the net macroscopic proton transport rate by ~twofold (*10*, *11*). In order to elucidate the mechanisms underlying this regulation, we characterized the activity of the proton pump with and without the R domain. Counterintuitively, the autoinhibitory R domain increased the total time the transporter spent in the active state, both by increasing t_{on} ~threefold (from 337 to 951 s, $P = 10^{-19}$) and by decreasing t_{off} ~0.5-fold (from 121 to 65 s, $P = 0.05$) (decay constants of exponential fits to the distributions in Fig. 3, F and G; unless otherwise stated, P is a Kolmogorov-Smirnoff test of statistical similarity between two distributions). Thus, the probability of finding the pump in an active state $P_{on} = t_{on}/(t_{on} + t_{off})$ increased ~200% for AHA2 (from 0.35 ± 0.05 to 0.76 ± 0.06). Importantly, 100% of $AHA2^R$ and ~60% of AHA2 molecules switched on/off during our observation period, highlighting the fact that functional dynamics is a dominant property of this system (Fig. 3F). The R domain also had a pronounced effect on the overall intrinsic transport rates of the pump, which were reduced by ~10-fold as compared to $AHA2^R$ (from 928 to 85 protons/s, average values, $P = 10^{-20}$) (Fig. 3E). In addition, the R domain promoted an overall decrease in the transprotein leak (~1.4-fold, $P = 0.005$) (Fig. 3D).

The activity of the pump was also regulated by the pH gradients established across the membrane during proton pumping. Increasing ΔpH_{max} decreased by >twofold the lifetime of the active state, but only for the wild type (Fig. 4A, B). This regulation seems to be transmitted allosterically across the bilayer, because the R domain of AHA2 is facing the vesicle exterior, where the pH remains constant. In addition, traces with larger ΔpH_{max} had a dramatic eightfold increase (from 0.1 to 0.8) in the probability of a transprotein leak for both forms of AHA2 (Fig. 4C). Thus, regulation by pH gradients can manifest through two mechanistically distinct processes that reduce the net average proton transport: reduction of the pumping lifetime and increase of the probability of a transprotein leak, whereby only the former is encoded in the R domain.

Our observations of proton transport and leakage dynamics at the single-molecule level also provide critical insights into the ATP/H^+ stoichiometry (*27*, *28*). Ensemble average experiments have reported that the buildup of pH gradients can in general alter the stoichiometry of transport and therefore pumping rates (*27*, *28*). Contrary to expectation, we found that the intrinsic (single-molecule) pumping rate remained constant for gradients as large as 2 pH units (Fig. 3, B and C, and fig. S12C). As discussed above, pH gradients did reduce the net proton transport, but primarily by increasing the probability of a downhill transprotein leak (Fig. 4C). However, because the transprotein leak takes place once the pump has switched to the inactive state (Fig. 3C, S9), it does not affect the actual stoichiometry of active transport. In contrast, the R domain reduced the intrinsic pumping rates by ~10-fold (Fig. 4E). Because the R domain does not significantly affect the ensemble average ATPase activity (*10*, *29*), our measurements suggest that the R domain can reduce the stoichiometry of active transport by a factor of ~10 (or 20 if we correct for the change in P_{on}) (*11*). Finally, we note that our measurements of proton transport were integrated over thousands of Post-Albers catalytic cycles per second per single molecule. A better mechanistic understanding of these processes would ultimately require direct measurement of the stoichiometry at the level of single turnover cycles or careful molecular simulations.

We have developed a technique to observe, in a highly parallel manner, uphill substrate transport mediated by single transporter molecules into single nanoscopic lipid vesicles. Our measurements revealed the existence and the dynamics of several distinct functional states (active, inactive, and leaky) that together defined the activity and regulation of the proton pump, and that, we anticipate, underlie the operation of many other primary and secondary active transporters. The assays introduced here render these processes accessible to direct experimental observation.

REFERENCES AND NOTES

1. F. Ashcroft, D. Gadsby, C. Miller, *Philos. Trans. R. Soc. London Ser. B* **364**, 145–147 (2009).
2. E. Neher, B. Sakmann, *Nature* **260**, 799–802 (1976).
3. J. P. Morth *et al.*, *Nat. Rev. Mol. Cell Biol.* **12**, 60–70 (2011).
4. L. J. DeFelice, T. Goswami, *Annu. Rev. Physiol.* **69**, 87–112 (2007).
5. R. Peters, *Annu. Rev. Biophys. Biomol. Struct.* **32**, 47–67 (2003).
6. A. Tonnesen, S. M. Christensen, V. Tkach, D. Stamou, *Biophys. J.* **106**, 201–209 (2014).
7. R. Watanabe *et al.*, *Nat. Commun.* **5**, 4519 (2014).
8. M. Li *et al.*, *J. Am. Chem. Soc.* **137**, 16055–16063 (2015).
9. B. P. Pedersen, M. J. Buch-Pedersen, J. P. Morth, M. G. Palmgren, P. Nissen, *Nature* **450**, 1111–1114 (2007).
10. M. G. Palmgren, C. Larsson, M. Sommarin, *J. Biol. Chem.* **265**, 13423–13426 (1990).
11. M. G. Palmgren, P. Nissen, *Annu. Rev. Biophys.* **40**, 243–266 (2011).
12. See materials and methods and supplementary information on *Science* Online
13. S. Mathiasen *et al.*, *Nat. Methods* **11**, 931–934 (2014).
14. P. M. Bendix, M. S. Pedersen, D. Stamou, *Proc. Natl. Acad. Sci. U.S.A.* **106**, 12341–12346 (2009).
15. D. Stamou, C. Duschl, E. Delamarche, H. Vogel, *Angew. Chem. Int. Ed. Engl.* **42**, 5580–5583 (2003).
16. G. C. Kemmer *et al.*, *Analyst* **140**, 6313–6320 (2015).
17. L. Iversen *et al.*, *Science* **345**, 50–54 (2014).
18. M. J. Comstock *et al.*, *Science* **348**, 352–354 (2015).
19. T. Yanagida, Y. Ishii, Eds., *Single Molecule Dynamics in Life Science* (Wiley-VCH, Weinheim, Germany, 2009).
20. X. S. Xie, in *Single Molecule Spectroscopy in Chemistry, Physics and Biology*, A. Graslund, R. Rigler, J. Widengren, Eds. (Springer-Verlag Berlin, 2010), vol. 96, pp. 435–448.
21. N. Akyuz *et al.*, *Nature* **518**, 68 (2015).
22. C. E. Aitken, J. D. Puglisi, *Nat. Struct. Mol. Biol.* **17**, 793–800 (2010).
23. G.-W. Li, E. Oh, J. S. Weissman, *Nature* **484**, 538–541 (2012).
24. A. R. Subramaniam, B. M. Zid, E. K. O'Shea, *Cell* **159**, 1200–1211 (2014).
25. B. Sakmann, E. Neher, Eds., *Single-Channel Recording* (Springer, New York, ed. 2, 2009).
26. M. Grabe, G. Oster, *J. Gen. Physiol.* **117**, 329–344 (2001).
27. M. C. Berman, *Biochim. Biophys. Acta* **1513**, 95–121 (2001).
28. N. Nelson, A. Sacher, H. Nelson, *Nat. Rev. Mol. Cell Biol.* **3**, 876–881 (2002).
29. M. G. Palmgren, M. Sommarin, R. Serrano, C. Larsson, *J. Biol. Chem.* **266**, 20470–20475 (1991).

ACKNOWLEDGMENTS

This work was supported by the Lundbeck Foundation (Center of Excellence Biomembranes in Nanomedicine); the Danish Councils for Independent (grant number 1323-00297) and Strategic Research; the Danish National Research Foundation (Center of Excellence PUMPKIN, grant number DNRF85); the University of Copenhagen programs of excellence Single Molecule Nanoscience, BioScaRT, and UNIK-Synthetic Biology; and the National Institutes of Health (grant number R21-GM100224). We are grateful to M. G. Palmgren, J. Mindell, and P. Nissen for stimulating discussions and comments on the manuscript; M. G. Palmgren for generously providing plasmids; U. Gether for instrumentation; and A.-M. Bjerg Petersen for excellent technical assistance. D.S. conceived the strategy and was responsible for the overall project supervision. B.H.J. performed cloning. G.C.K., B.H.J., and I.L.J. expressed, purified, and reconstituted $AHA2^R$ and AHA2 and performed macroscopic measurements and data analysis under the supervision of T.G.P. T.G.P. synthesized and G.C.K purified pHrodo-PE; J.S. performed and analyzed mass spectrometry experiments of pHrodo-PE. S.M.C. wrote software for analyzing time-lapse sequences of single vesicles. S.V. designed, performed, and analyzed most single-vesicle experiments, with help from M.P.M and G.G., under the supervision of S.M.C. and D.S.. C.L., A.L.C., and N.S.H. contributed with preliminary single-vesicle acidification measurements. M.G. contributed the model of vesicle acidification. D.S. wrote the manuscript, and S.V., G.G., M.P.M., B.H.J., G.C.K., I.L.J., and T.G.P. helped prepare figures and supplementary materials. All authors discussed the results and commented on the manuscript.

SUPPLEMENTARY MATERIALS

www.sciencemag.org/content/351/6280/1469/suppl/DC1
Materials and Methods
Supplementary Text
Figs. S1 to S12
Tables S1 and S2
References (*30*–*47*)

15 October 2015; accepted 23 February 2016
10.1126/science.aad6429

Direct observation of proton pumping by a eukaryotic P-type ATPase

Salome Veshaguri *et al.*

Science **351**, 1469 (2016);
DOI: 10.1126/science.aad6429

www.sciencemag.org/content/351/6280/1469/suppl/DC1

Supplementary Materials for

Direct observation of proton pumping by a eukaryotic P-type ATPase

Salome Veshaguri, Sune M. Christensen, Gerdi C. Kemmer, Garima Ghale, Mads P. Møller, Christina Lohr, Andreas L.Christensen, Bo H. Justesen, Ida L. Jørgensen, Jürgen Schiller, Nikos S. Hatzakis, Michael Grabe, Thomas Günther Pomorski, Dimitrios Stamou*

*Corresponding author. E-mail: stamou@nano.ku.dk

Published 25 March 2016, *Science* **351**, 1469 (2016)
DOI: 10.1126/science.aad6429

This PDF file includes:

Materials and Methods

Chemicals

Phospholipids were used as received from Avanti Polar Lipids Inc. (Birmingham, AL, USA). L-α-Phosphatidylcholine (soybean, Type II-S, 14-23% choline basis) was purchased from Sigma-Aldrich (Brøndby, Danmark). Detergent n-Dodecyl-β-D-maltoside (DDM) was obtained from Glycon Biochemicals (Luckenwalde, Germany). Unless indicated otherwise, all other chemicals and reagents were obtained from Sigma-Aldrich (Brøndby, Danmark).

The lipid-conjugated pH-sensor PE-pHrodo

The lipid conjugated pH sensor PE-pHrodo was synthesized by linking DOPE to the commercially available pHrodo™ red ester reagent (Invitrogen, Eugene, OR, USA). Synthesis, purification and characterization of its spectral properties as a function of pH are described in detail in reference (*16*).

Liposome preparation

Unilamellar liposomes were prepared by manual extrusion. Briefly, chloroform stocks of L-α-phosphatidylcholine (12.7 μmol), biotinylated lipid (DOPE-biotin, 38 nmol; 0.3 mol%), and lipid-linked pHrodo sensor (20 nmol; 0.15 mol%) were dispensed into a round bottom flask, mixed, and dried by rotary evaporation, followed by incubation for 1 h under vacuum. The lipid film was rehydrated in 667 μl of reconstitution buffer (10 mM Mes-KOH, pH 6.5, 50 mM K_2SO_4, 20% glycerol), dissolved by vortexing in presence of a glass pearl, and passed through 0.2 μm size nucleopore polycarbonate membranes mounted in a mini-extruder (Avanti Polar Lipids, Alabaster, AL). The resulting liposomes were kept at 4°C and used within 1 week.

Protein expression and purification

Arabidopsis thaliana H^+-ATPase isoform 2 wild type (AHA2) and its 73 amino acid C-terminal truncated variant ($AHA2^R$) were expressed and purified according to previously published protocols (*30*).

Briefly, a plasmid based on the multicopy vector YEp-351 (*31*) was used for expression in yeast, containing the coding sequence of AHA2 (with a SNAP coding sequence and a MRGSH6 tag at the N-terminus) or $AHA2^R$ (with a C-terminal MRGSH6 tag). Protein expression and purification were performed using *Saccharomyces cerevisiae* strain RS-72 (MATa ade1-100 his4-519 leu2-3,112) (*32*) as expression host. Cells were transformed and cultured essentially as described previously (*33*). In RS-72 the endogenous yeast H^+-ATPase PMA1 gene is placed under the control of a genomic galactose-dependent promoter. This strain grows in media containing galactose while growth in glucose based medium requires the complementation of the yeast H^+-ATPase by the constitutively expressed *A. thaliana* H^+-ATPase. The cells were grown, harvested by centrifugation, and membranes isolated as described previously (*9*). All subsequent manipulations were performed at 4°C, and all buffers contained 0.3 mM phenylmethylsulfonyl fluoride and 3 μg/ml pepstatin A. Membranes were solubilized using DDM at a 3:1 detergent:protein (w/w) ratio in solubilization buffer (50 mM Mes-KOH, pH 6.5, 20% (v/v) glycerol, 1 mM EDTA, 50 mM KCl, 1 mM dithiothreitol)

containing 1.2 mM ATP with gentle agitation for 30 min. Insoluble material was removed by centrifugation for 60 min at 100,000 × g. The supernatant containing solubilized *A. thaliana* H^+-ATPase was diluted 1:1 (v/v) with washing buffer WB500 (50 mM Mes-KOH, pH 6.5, 20% (v/v) glycerol, 0.15% (w/v) DDM, 500 mM KCl, 10 mM imidazole), and incubated for 16 h with Ni^{2+}-NTA resin (1 ml of resin, 30 mg membrane protein) pre-equilibrated in the same buffer. To minimize unspecific binding, the Ni-NTA resin was washed with 10 volumes of washing buffer WB250 (as WB500 with 250 mM KCl) followed by 10 volumes of washing buffer WB50 (as WB500 with 50 mM KCl). Bound proteins were eluted with 2 volumes of elution buffer (50 mM Mes-KOH, pH 6.5, 50 mM KCl, 300 mM imidazole, 20% (v/v) glycerol, 0.5 mM dithiothreitol, and 0.04% (w/v) DDM). Centrifugal concentrators (Vivaspin 20, GE Healthcare) with 30 kDa molecular mass cut off were used for buffer exchange of the eluted proteins to solubilization buffer containing 0.04% (w/v) DDM in two washing steps. Purified H^+-ATPase was finally concentrated to 1-10 g/l, frozen in liquid nitrogen and stored at -80°C.

Proteoliposome reconstitution, characterization, and AHA2 labelling

Purified H^+-ATPase was reconstituted into preformed liposomes as described earlier (*30*). Briefly, using the indicated amount of purified protein in 220 µl reconstitution buffer containing 50 mM octylglucoside (OG) and liposomes (3 µmol phospholipid). The solubilized protein/lipid/detergent mixture was subjected to gel filtration (Sephadex G-50 Fine, 2 ml packed in 2 ml disposable syringes) by centrifugation (180 × g, 7 min). The eluate was incubated for 30 min at room temperature with 100 mg of wet Bio-Beads (Bio-Beads SM-2, Bio-Rad) under overhead rotation to eliminate traces of detergent. Protein-free liposomes were prepared accordingly by replacing purified protein with reconstitution buffer.

The unilamellarity and size of proteoliposomes were characterized with a cryogenic transmission electron microscope (Cryo-TEM). Typical cryo-TEM micrographs of proteoliposomes (fig. S3). Cryo-TEM was performed at Biomikroskopienheten, Materialkemi, Kemi Centrum, University of Lund, Sweden using a Philips CM120 (BioTWIN Cryo) equipped with a GATAN CCD camera (1024 × 1024 pixels). Occasionally the less informative ensemble average technique of dynamic light scattering was used to confirm size distributions.

AHA2-proteoliposomes were labelled using a 2-fold excess of substrate SNAP-Surface® Alexa Fluor®647 (New England Biolabs) to enzyme (SNAP-AHA2) concentration according to manufacturer's instructions (New England Biolabs). The amount of reconstituted AHA2 in the proteoliposomes was estimated by assuming a 100% rate of recovery throughout reconstitution. The labeling reaction was carried out in the dark for 30 min at 37°C. Orientation of AHA2 in the proteoliposomes was determined by a trypsin protection assay (fig. S2C). The proteoliposomes (10 µl) were treated with trypsin (0.1 mg/ml) for 30 min at 30°C. The digestion was stopped by the addition of SDS loading buffer. Samples were analyzed by SDS-PAGE using 12% gels and visualized by fluorescent scan (λ_{ex} = 652 nm, λ_{em} = 670 nm) and Coomassie Brilliant Blue staining (λ_{ex} = 633 nm) using a Typhoon Scanner (GE Healthcare). Bands were quantified by densitometry using either the GelQuant.NET software provided by biochemlabsolutions.com or Image Lab™ Software from Bio-Rad. The degree of

labeling was investigated by proteolytic assays using TEV protease. The proteoliposomes (30 µl) were treated with TEV protease (0.33 mg/ml) for 30 min at 30°C and subjected to SDS-PAGE analysis along with standards of known amounts of AHA2 and SNAP-Surface® Alexa Fluor® 647 labelled SNAP protein (fig. S2D). Efficiency of the TEV digestion was calculated by comparing fluorescent levels of AHA2 bands before and after TEV digestion. Based on the AHA2 standard, the TEV digestion efficiency, and the amount of AHA2 digested by the TEV protease, the total amount of outward oriented AHA2 in the proteoliposomes was estimated (fig. S2D). The amount of fluorescent SNAP tag cleaved off from AHA2 ($SNAP^{TEV}$), was estimated based on the fluorescent SNAP protein standard. From the TEV digestion efficiency, the amount of fluorescent $SNAP^{TEV}$ was used to calculate the total amount of labeled AHA2 protein. The labeling efficiency was calculated as the amount of labeled AHA2 out of total outward oriented AHA2, and given in percentage.

Bulk activity assays and ATP permeability of liposomes

Bulk proton pumping activity was measured with a spectrofluorometer at 25°C using a Fluoromax-4 spectrofluorometer (Horiba, Edison New Jersey, USA) equipped with a LFI-3751 temperature controller (Wavelength Electronics, Bozeman, MT, USA). Proteoliposomes (5 µl) were added to 1 ml transport buffer (20 mM MOPS-KOH, pH 6.5, 52.5 mM K_2SO_4) containing 2 mM ATP and 60 nM valinomycin. If not stated otherwise proton pumping was initiated by the addition of $MgSO_4$ to a final concentration of 2 mM, and when indicated dissipated by the addition of 5 µM Carbonyl cyanide m-chlorophenylhydrazone (CCCP). Fluorescence traces were recorded at 590 nm for 600 s (excitation, 532 nm; slit widths, 4 nm; resolution, 0.1 s).

ATPase activity was determined at pH 7 by measuring the formation of inorganic phosphate Pi using a malachite green colorimetric ATPase assay in a reaction mixture comprising ATPase buffer (20 mM MOPS-KOH, pH 7, 8 mM MgSO4, 3 mM ATP) at 30°C. When solubilized H^+-ATPase was analyzed, the buffer contained 0.5% (w/v) L-α-Phosphatidylcholine and 0.05% (w/v) DDM. For the calculation of the amounts of released phosphate, the absorbance was compared to the absorbance of a phosphate standard curve using a spectrophotometer (Ultrospec 2000, Pharmacia Biotech). The average specific ATPase activities measured for $AHA2^R$ and AHA2 were 14.9 ± 5.3 µmol Pi/min/mg (n=7) and 16.2 ± 8 µmol Pi/min/mg (n=5) respectively.

To measure the passive membrane permeability of ATP we performed leakage experiments of radiolabeled ATP ([γ-32P]-ATP, PerkinElmer, Boston, MA, USA) from proteoliposomes. $AHA2^R$ (75 µg) was reconstituted in extruded liposomes (99% L-α-Phosphatidylcholine, 1% L-α-Phosphatidylethanolamine-N-lissamine rhodamine B sulfonyl [Rhodamine-PE], Avanti Polar Lipids Inc., Birmingham, AL, USA) in the presence of ATP (5 µCi [γ-^{32}P]-ATP, 2 mM ATP). Proteoliposomes (200 µL) were mixed with transport buffer (800 µL) supplemented with 60 nM valinomycin, and incubated at room temperature. To remove released ATP, aliquots (220 µL) were taken at indicated time points (see table S1) and subjected to gel filtration (Sephadex G-50 Fine, 2 ml packed in 2 ml disposable syringes) by centrifugation (180 g, 7 min). Radioactivity of the eluates (180 µL in 2 mL scintillation fluid (Optiphase HiSafe 3, PerkinElmer, Boston, MA, USA) was counted on a 1450 MicroBeta Wallac TriLux Counter (PerkinElmer Life Sciences, Skovlunde, Denmark). Radioactivity was normalized to Rhodamine-PE

fluorescence intensity of eluates (5 µL in 1 mL transport buffer supplemented with valinomycin), measured in a Fluoromax-4 spectrofluorometer at 25°C, with excitation at 560 nm (slit width 3 nm) and emission recorded between 570 and 700 nm (slit width 3 nm). A control reconstitution in the absence of ATP was performed simultaneously and radioactivity counted used as buffer correction. Functional reconstitution was confirmed by the 9-amino-6-chloro-2-methoxyacridine (ACMA) quenching assay. Under conditions used here, 1% of the 2 mM ATP can pass the lipid bilayer in the first hour of incubation (typical time course of an experiment). These numbers are in excellent agreement with published results (*34*). We note, that since in this assay we cannot discriminate and correct for non-specific binding to the outer leaflet of the bilayer 0.02 mM /hr or ~10^{-5} mM /s is an upper limit.

Passive ATP leakage is not fast enough to fuel pumps oriented inside/in: the fast leakage rates are ~100 H^+ /s or ~0.1 mM /s (for an average sized vesicle ~100 nm in diameter). Thus, since the proton leakage rates are ~100,000 times faster than the upper-estimate of passive ATP leakage we can exclude conclusively the possibility that fast leakage is due to ATP-fuelled activity of pumps oriented inside/in. Actually, at a concentration of 10^{-5} mM ATP cannot even bind to the proton pump that has an apparent ATP affinity ~2 mM or ~0.1 mM respectively for the wild type (*33, 35*) and for $AHA2^R$ (*36-38*).

Surface preparation and Immobilization of AHA2 vesicles

To prepare surfaces for microscopy measurements we followed verbatim protocols from our lab that have been previously published and validated (*13*).

Briefly, flow cells were prepared by assembling sticky slides VI0.4 purchased from Ibidi and passivated glass slides. Prior to their use, glass slides (thickness 170 ± 10 µm) were sonicated repeatedly in 2% (v/v) Helmanex, 70% (v/v) ethanol, and Milli-Q water (MQ; Millipore). The slides were dried under nitrogen flow and plasma etched for 2 minutes and then immediately assembled with the flow cell. The flow cell was then incubated with a mixture of 1000:6 PLL-g-PEG and PLL-g-PEG-biotin (SuSoS) (1 g/l) in surface buffer (15 mM HEPES, pH 5.6). After 30 minutes, the flow cell was washed with surface buffer and subsequently incubated (10 minutes) with 0.1 g/l NeutrAvidin (Life Technologies). The unbound NeutrAvidin was removed by flushing the flow chambers with transport buffer (20 mM MOPS, 52.5 mM K2SO4, 60 nM valinomycin, pH 6.5).

Proteoliposomes were immobilized on a passivated glass surface in flow cells or home-built microscopy chambers by exchanging the transport buffer in the flow cells with proteoliposome (3.5–7 mg/l) solution until the surface density reached approximately ~1000 proteoliposomes per frame. Proton pumping was initiated by the injection of ATP and Mg_2SO_4 (2 mM final concentrations) to the flow cell and when indicated dissipated by the addition of 5 µM Carbonyl cyanide m-chlorophenylhydrazone (CCCP).

Image acquisition

Fluorescence intensity was measured with a total internal reflection fluorescence (TIRF) microscope (Nikon N-Storm, Nikon Instruments Inc., Melville, NY, USA) equipped with an EMCCD camera (Andor Technology, Belfast, UK). A solid state laser (Coherent Inc., Santa Clara, CA, USA) with an excitation wavelength of 561 nm was

used to excite pHrodo. Microscope was equipped with CFI Apo TIRF 100X Oil immersion objective (1.49 NA, Nikon, Japan). The microscope has a built-in perfect focusing system, which allows real-time focus control and was used during all experiments. Excitation of PE-pHrodo was filtered out using excitation band-pass filter ET560/40. Emission was detected in the range of 592.5 – 667.5 nm using emission band-pass filter ET630/75, with laser-beamsplitter zt561RDCXT. Images were acquired in the format of 512 × 512 pixels, each pixel corresponding to 160 nm sample length, bit depth of 14, with readout speed of 10 MHz. Filters and beam splitters were purchased from Analysentechnik AG, Tübingen, Germany. Laser power for 561 nm laser line was measured before each experiment in front of objective and was set to 4.2 or 2.6 μW depending on sample labelling efficiency. A solid state laser (Coherent Inc., Santa Clara, CA, USA) with an excitation wavelength of 647 nm was used to excite Alexa Fluor®647. Emission was detected in the range of 662.5 – 737.5 nm using emission filter BA700/75, with laser-beamsplitter DM660.

Image analysis and size calibration

Microscopy data were analysed using a software suite developed in Igor Pro ver. 6.22A. Single particle localization and quantification of fluorescence intensities was achieved as described elsewhere (*13, 39*). Briefly, particle positions were identified by localizing sites of divergence in the gradient vector field of the micrographs(*39*). The integrated fluorescence intensity was then obtained for each particle by fitting the intensity profile with a two-dimensional Gaussian function (Gauss 2D fit function in Igor Pro) (fig. S5).

Single transporter kinetics were acquired as an image time series. Each kinetic recording was supplemented with additional image data, acquired for the same set of liposomes, to measure the size of each liposome(*40*) and its own pH response curve (fig. S5). An image of the liposome membrane marker functioned as a mask for defining particle positions. Based on the mask image, kinetic traces were obtained by integrating the volume under a 2D Gaussian fit in an 11 by 11 or 9 by 9 pixels region of interest (ROI) centred at each liposome. (fig. S5). Traces with transporter kinetics for single liposomes bundled with the fluorescence intensity observed in the size determination image and the pH titration series were then saved for further processing.

Analysis of kinetics to identify transport activity events was accomplished via a graphical user interface (GUI). A batch of single transporter activity traces was loaded and conversion of fluorescence intensity to pH was achieved using the calibration curve particular to a given liposome.

To identify transport events, traces were first smoothed (200 binomial smoothing operations), then differentiated. The differentiated traces were smoothed (100 binomial smoothing operations) and raised to the third power.

Transport events were now located by searching the resulting differentiated trace for crossing of a user-defined threshold (defined via the GUI). The time point of crossing the threshold was taken as an initial estimate for the onset of a transport event, t_{start}. Next, the search was continued, this time to locate a crossing of the negative of the threshold value. This time point was taken as an initial estimate for the onset of proton leakage (if any), t_{peak}. Finally, the search was continued to locate a crossing of the value 0. This time point was taken as an initial estimate for the termination of the leakage event, t_{end}. The search

was continued, repeating the cycle above, to locate all transport events in a trace. The integrity of event localization was visually verified by the user of the GUI and, where necessary, the threshold was adjusted to ensure proper event assignment (fig. S5).

To refine the initial estimate for the transition time points t_{start} and t_{end} we employed the derivative of the differentiated trace used for the search cycles above (i.e., the acceleration of the original trace). t_{start} and t_{end} were updated to correspond to the respective nearest local maxima in the acceleration trace.

The estimate for the peak position was refined by fitting one exponential function to the part of the trace defined by t_{start} and t_{peak} and another exponential to the part of the trace defined by t_{peak} and t_{end}, respectively. t_{peak} was iterated from t_{start}+4 to t_{end}-4. For each iteration, the residuals for the whole event were calculated. The best estimate for t_{peak} was taken as the one that minimized the residuals.

Finally, the peak plateau of each transport event, I_{peak}, was determined as the average of the 4 data points just prior to t_{peak} and the value at t_{peak}. Similarly, the base level of the transport event was calculated as the average of 5 data points before t_{start}.

The sizes of proteoliposomes were calculated as described previously(*40*). Briefly, number of PE-pHrodo fluorophores incorporated in the membrane is proportional to the proteoliposome surface area ($A_{liposome}$) and thereby related to diameter ($D_{liposome}$) through equation (1), a conversion from diffraction-limited intensity spots to physical proteoliposome size was possible.

$$I_{PE-pHrodo} \propto A_{liposome} = 4\pi R_{liposome}^2 \Longrightarrow R_{liposome} = k\sqrt{I_{PE-pHrodo}} \quad (1)$$

The calibration factor (k) was determined by testing reconstituted AHA2 proteoliposomes extruded at 200 nm filters. To obtain the mean radius of AHA2 proteoliposomes the sample was examined by using CRYO-TEM microscopy (Fig. S3). To calculate k, the proteoliposomes were initially imaged in wide-field mode before triggering of the transport reaction. From these images, the mean of the integrated PE-pHrodo intensity spots were determined. This value was correlated to the mean radius found by CRYO-TEM to obtain k. After determination of k, all intensities were converted to diameters by using equation (1).

The signal-to-noise ratio (SNR) for single vesicle activity traces was calculated as

$$SNR = (I_{max} - 1)/s \quad (2)$$

where I_{max} is the highest peak plateau of the normalized single vesicle activity trace and s is the standard deviation of the baseline before injection of ATP and Mg^{2+}.

<u>Calculating the number of active AHA2 molecules per vesicle using bleaching step counting analysis</u>

Since we were able to express, purify and reconstitute functional AHA2 in fusion with a SNAP tag, we were also able to label it fluorescently and count directly the number of proteins per vesicles using bleaching step counting analysis. As described below, the number of labeled proton pumps was corrected for labeling efficiency and the probability to be active, in order to finally obtain the histogram of active molecules per vesicle (Fig. 2F).

<u>Colocalization analysis.</u> To identify proteoliposomes i.e. exclude protein aggregates and liposomes (with no protein) we colocalized the signal from AHA2 labelled with

Alexa Fluor®647 (Alexa647-AHA2) and liposomes labelled with pHrodo-PE. The reconstitution and labelling process is described in Section 5. First, surface immobilized liposome micrographs (pHrodo-PE channel) were acquired, followed by recording of Alexa fluor®647 bleaching movies for the same set of liposomes. Afterwards, spatially overlapping/colocalized signals were identified from the separate colour channels. Intensity signals were determined for each fluorescent label and an x,y centre position was assigned for all diffraction-limited intensity spots. Colocalization was defined as particles in separate colour channels having centres within a distance of 2 pixels. To estimate non-specific binding of Alexa fluor®647 on vesicles we have tested mock liposomes treated similar to Alexa647-AHA2 proteoliposomes (described in Section 5). We found that non-specific binding is not significant as less than 0.4% of the entire liposome population showed overlapping signals from the Alexa fluor®647 channel. In total, 6191 liposomes from 2 independent experiments (8 different fields of view each) were tested. 870 or 17±5% (n=2) showed overlapping signals between Alexa fluor®647 and pHrodo-PE channels and were thus identified as proteoliposomes.

Step bleaching analysis. Positions with colocalized signals were used to extract bleaching traces of Alexa fluor®647. To count AHA2 copies per liposome bleaching step-counting analysis was performed. Distinct bleaching steps of Alexa fluor®647 were fitted using a change point localization algorithm (the modality for Gaussian processes described in the reference(*41*)). A Bayes factor of 10 was applied as a criterion in change point detection. As an additional filter, only change points where the difference between adjacent intensity plateaus exceeded five times the sum of the standard error of the two intensity means were accepted as significant $(|I_2-I_1|>3(SEM_1+SEM_2)$, where I indicates the intensity average of the respective plateaus and SEM the corresponding standard error). 62±3% of the colocalized proteoliposomes showed single step bleaching of Alexa fluor®647 attached to a single AHA2 transporter. 19±2% of proteoliposomes showed two bleaching steps, while the remaining 19±1% showed more than two bleaching steps.

Estimation of the probability of a proton pump to be active. In order to estimate the fraction of functional AHA2 molecules we have performed parallel colocalization and activity/acidification measurements for Alexa647-AHA2 reconstituted proteoliposomes. We found that 62±11 % (N=2) of liposomes with protein showed acidification of the lumen facilitated by an active Alexa647-AHA2. Thus the remaining ~38% of proteoliposomes carry inactive AHA2. Next we calculated the distributions of Alexa fluor®647 bleaching steps for the active and inactive proteoliposomes separately. We found that the two distributions are similar within experimental errors (61±4% and 55±4% showed one bleaching step; 27±3% and 29±6% showed two bleaching steps, 12±1% and 16±9% and showed more than two bleaching steps for active and inactive proteoliposomes respectively). Thus, fraction of inactive proteoliposomes corresponds to a fraction of inactive proton pumps. Therefore, the probability of a proton pump to be active after purification and reconstitution is 0.6±0.1.

Estimation of the labeling efficiency from single molecule experiments. To calculate the labeling efficiency of AHA2 at the single vesicle level and compare the results with bulk values (see Fig. S2) we screened for the liposomes that showed lumen acidification without detected overlapping signals from Alexa fluor®647 channel. Under the assumption that the number of acidified liposomes would also represent ~62% of the total non-labelled AHA2 proteoliposomes we estimated the labeling efficiency to be 56 ± 9%

(N=2). This result was in a good agreement with bulk measurements giving a labeling efficiency of 53 ± 12% (see Fig. S2). In total 1676 liposomes were tested for analysis in subsections 10c and10d.

Finally, to obtain the probability of observing 1, 2, or more active AHA2 molecules per liposome in main Figure 2F we used the following equation (3):

$$P_{Active\ AHA2} = \frac{Occurence_{Number\ of\ bleaching\ steps}\ *P_{AHA2\ being\ active}}{Alexa\ fluor®647\ labelling\ efficiency\ of\ AHA2} \quad (3)$$

Error bars in main Figure 2F represent propagated errors.

Calibration of pH inside vesicles

Bulk. Bulk calibration was performed by diluting 3.3 µL liposomes in 1 mL of buffers at different pH between 2.7 and 8 (20 mM phosphate buffer supplemented with 20 mM citrate where applicable, 52.5 mM K2SO4, 60 nM valinomycin, 5 µM CCCP). Liposomes were equilibrated for at least 15 min at room temperature before measurements (Ex. 532 nm, Em. 550-700 nm) in a Fluoromax-4 spectrofluorometer (Horiba, Edison New Jersey, USA) equipped with a LFI-3751 temperature controller (Wavelength Electronics, Bozeman, MT, USA); experiments were performed at 25°C. Traces were inspected for changes in overall shape and absolute intensity values normalized to the maximum at pH 3 (fig. S6 E–G). Calibration curves were obtained by plotting normalized intensities at the maximum against buffer pH and fitting a sigmoidal function (fig. 6E). For kinetic measurements, absolute intensity values were subtracted by half of the average baseline intensity, as the outside monolayer does not contribute in H^+ specific intensity change in the lumen of the proteoliposome. Baseline was defined by intensity values acquired before injections.

Single vesicles. After immobilization of AHA2 proteoliposomes on the passivated glass surface, 5 consecutive wide-field images were acquired to calculate the size of each individual proteoliposome. Subsequently, a sequential imaging of the selected position was started and after approximately 60 s, ATP (2 mM) and Mg^{2+} (2 mM) were injected.

After single vesicle activity assays, the pH gradients in proteoliposomes were collapsed by adding a protonophore, carbonyl cyanide-m-chlorophenylhydrazone (CCCP, 5 µM). This step was followed by the exchange of transport buffer with citrate–phosphate buffers of varying pH (7.3–2.7) in presence of valinomycin (60 nM). For each pH value 9 consecutive images of each individual proteoliposomes were recorded to obtain the average ± s.d. Since the outside monolayer of a proteoliposome does not contribute in H^+ specific intensity change in the lumen of the proteoliposome, we subtracted half of the average baseline intensity from the total absolute intensity values of individual proteoliposomes. Baseline was defined from the images acquired before Mg^{2+} and ATP injection.

Of all the vesicles containing single transporters, and which were relevant to our experiments, 20-30% could not be analysed quantitatively for entirely technical reasons. Typical technical problems were: A) Vesicle traces with multiple switches between active/inactive states that ended by being active were not analysed due to a limitation/bug in the current version of the software. B) Bleaching was critical dependent on pH, thus for vesicles that oscillated between different pH values bleaching corrections were non-trivial to implement. Therefore vesicles that bleached more than ~2% of their total

intensity were excluded from analysis. C) Vesicles for which the pH calibration curves did not converge.

Determination of passive proton leakage in single vesicles

Leakage experiments were performed to reveal the contributions of proton leak from passive diffusion through the lipid membrane and in particular, through the protein $AHA2^R$ (*cf*. Figure 2 and 3 in main text) during pumping activity. In detail, liposomes and $AHA2^R$-reconstituted proteoliposomes were prepared exactly as described in Materials and Methods using reconstitution buffer set at pH 5. Note, the liposomes ($AHA2^R$ absent) are subjected to the exact same preparation or treatment as $AHA2^R$-reconstituted liposomes. The vesicles were incubated with valinomycin (60 nM) prior to their immobilization to a glass surface in a flow cell (see Supplementary Information 7). After immobilization, unbound vesicles were flushed with transport buffer at pH 5. The leakage test was initiated by exchanging the buffer to pH 7 (fig. S10).

Upon exchanging the buffer of the solution from low (pH = 5) to high pH (pH =7) for both liposomes and proteoliposomes, two distinct kinetic phases were observed – a rapid drop in fluorescence intensity corresponding to the outer monolayer, followed by a relatively slow decrease in the signal corresponding to the inner monolayer (fig. S10E, F). For liposomes where the fluorophores were present exclusively in the outer monolayer, only a rapid drop in fluorescence signal was observed. The outer leaflet selective labeling of the vesicles was achieved by incubating preformed unlabelled vesicles with pHrodo labeled lipid (1.5 % DMSO, 60 minutes). The individual fluorescent traces were fitted to single (outer leaflet labelled vesicles) and double exponential decay (liposomes and proteoliposomes) functions to give a fast (τ_1) and slow (τ_2) decay lifetimes. Histograms were plotted from lifetimes and were fitted to single and double Gaussian function. The location of the peak for each Gaussian was used to determine the mean lifetime. For the fast decay component (τ_1) of liposomes and proteoliposomes, it can be seen that the histograms have a very similar mean distribution (fig. 10 A,D & G-I). As expected, this observation provided us with a confirmation that the initial drop in the fluorescence signal for liposomes and proteoliposomes were due to quenching of the fluorophores in the outer leaflet.

Following the decrease in fluorescence signal from fluorophores in the outer leaflet, in an ideal scenario, i.e., lipid membrane impermeable to ions, further decrease in fluorescence signal is not expected. However, the fluorescence intensity for both liposomes and inactive proteoliposomes (ATP and Mg^{2+} absent) continued to decrease (slow decay given by τ_2), indicating passive leakage of protons from the lumen of the vesicles (fig. S10 D–F)

In order to gain further understanding about the passive leakage of protons in $AHA2^R$-reconstituted proteoliposomes, we investigated the leakage lifetimes at various conditions (fig. S9). By comparing the histograms of leakage lifetimes between liposomes, and proteoliposomes that were active or inactive (i.e. in the presence or absence of ATP and Mg^{2+}) (fig. S9A–C) we were able to confirm that the significant portion of proton leak was indeed through the lipid bilayer (peak I in fig. S9). However, the active proteoliposomes had an additional leak state (peak II in fig. S9C), suggesting an alternate pathway for the passive flow of protons. Interestingly, the faster leakage observed for active proteoliposomes (peak II) was absent when the activity of $AHA2^R$

was inhibited by vanadate, fig. 9D. These observations allowed us to conclude that two possible leakage pathways exist for AHA2^R-reconstituted proteoliposomes, *i*) diffusion through the lipid membrane which is prominent and present in all conditions (passive membrane leak), and *ii*) leakage associated with the membrane protein AHA2^R (transprotein leak), which is present only when the pump is active.

Supplementary Text

Mathematical model of proton pumping and proton leakage in a vesicle

Here, we consider a vesicle containing a P-type proton pump, proton leak, and a potassium leak. Following our previous work on this topic (*26, 42*), a system of equations for the model are as follows:

$$\frac{dpH}{dt} = -\frac{1}{\beta(pH)} \cdot \frac{d[H^+]_T}{dt}$$

$$\frac{dH^+}{dt} = I_P - \left(P_{leak} S + q_{AHA2}\right) \frac{U\left([H^+] - [H^+]_0 e^{-U}\right)}{1 - e^{-U}}$$

$$[H^+] = 10^{-pH}$$

$$\frac{dK^+}{dt} = -P_K S \frac{U\left([K^+] - [K^+]_0 e^{-U}\right)}{1 - e^{-U}}$$

$$\psi = \frac{FV}{C_0 S}\left(\left([K^+] + \int_{pH_0}^{pH} \beta(pH)\, dpH\right) - B\right) \qquad (4)$$

where U is the reduced membrane potential ψ/k_BT, which is related to the net charge accumulated in the vesicle using a capacitor model for the membrane (*43*). We assume that the membrane potential outside the vesicle is zero. Bracketed quantities refer to molar quantities or concentrations, while unbracketed quantities are numbers. Hence, [X] = X/V, where V is the volume. H^+ is the total number of protons that *enter* the lumen, and a fraction of these ions become buffered. Proton pumping by AHA2 is represented by I_P, P_{leak} is the passive proton permeability of the membrane, P_{AHA2} is the passive proton permeability associated with AHA2 that can also be expressed as q_{AHA2} (an AHA2-dependent proton leak constant with units of permeability times area). The buffering capacity of the lumen (β) depends on the intracellular pH as discussed next. Both the volume (V) and the surface area (S) of the vesicle are assumed to remain fixed during the time course of acidification. Quantities without subscripts refer to intracellular values, while a zero subscript ($[\ldots]_0$) refers to extracellular, fixed values. The integral in the equation for the membrane potential is simply the sum of all charged protons that have entered the lumen during acidification, H^+_T. We set this value to zero at the beginning of all calculations, which essentially assumes that the protons near neutral pH do not significantly contribute to the resting membrane potential. Any trapped negative charges, MOPS and SO_4^{2-}, are modelled by a Donnan particle concentration (B), which is constant in time and set as described later. The K^+ permeability (P_K) is set to a large value since the presence of valinomycin in solution allows for fast shuttling of potassium across the

bilayer. Please refer to Fig. 3A of the main text for a cartoon model of this system, and table S2 for all values.

Proton pumping (I_P) is a time dependent quantity initiated at time t_{on} and then turned off at time t_{off}, where both times are determined for each experimental trace prior to solving the system of equations. The initial pH in the vesicle is set to the mean value of recorded pH from time zero to t_{on}, and the initial intracellular potassium concentration is then set such that the system starts at equilibrium. The system geometry is assumed to be spherical with the vesicle radius (R) derived from fluorescent intensity according to the equation 1. Once R is experimentally determined both V and S in Eqs. 4 are also defined. The equations are solved with Matlab (Natick, Massachusetts) using the ode15s stiff solver. Initial conditions for all time dependent variables are set as follows. The initial luminal pH value is set to the experimental value averaged from time zero to the start of the first pumping event. The initial luminal potassium concentration and the value B in membrane potential are then set so that the initial potassium flux and proton flux across the membrane is zero; hence, the system starts at steady state.

Buffer capacity.

According to Brönsted, an acid is any substance that is capable of donating a proton,

$$AH \leftrightarrow H^+ + A^-.$$

The equilibrium of this reaction is described by an equation of the form:

$$K = \frac{[H^+][A^-]}{[AH]},$$

where K is the equilibrium constant. This can be rewritten as:

$$pH = pK_a + \log_{10}\left(\frac{[A^-]}{[AH]}\right), \quad (5)$$

where $pK_a = -\log_{10}K$. The buffer capacity is defined as the ratio of the change in base to the change in pH:

$$\beta = \frac{\Delta[A^-]}{\Delta pH} \quad (6)$$

In a closed system, $[AH]+[A^-]=T$ is constant

$$[A^-] = \frac{T}{K + [H^+]}.$$

Combining Eqs. 5 and 6 and then taking the partial derivative of A^- with respect to pH with total buffer $[AH]+[A^-]$ constant, we find

$$\beta = \frac{\Delta[A^-]}{\Delta pH} = \frac{\Delta[A^-]}{\Delta[H^+]} \cdot \frac{\Delta[H^+]}{\Delta pH}$$

$$\Rightarrow \beta = 2.3 \cdot T \frac{K[H^+]}{\left(K + [H^+]\right)^2} \quad (7)$$

This last equation is used to determine the buffering in Eqs. 4. It has the property that buffering goes to zero when the proton concentration is far above the pK_a of the titratable group, and nearly all protons are buffered for concentrations far below the pK_a.

When more than one titratable group is present, as is the case for the current experiments, the buffering capacities are additive. For a more complete discussion of buffering in cellular systems refer to the work of Boron (*44*).

Fitting data.

The model was fitted to the experimental data using a Nelder-Mead search algorithm. Either three parameters were varied during the search (P_{leak}, I_P, q_{AHA2}) or two parameters (P_{leak}, I_P). The score of each fit is the sum of the square of the difference between the model pH value and the experimental pH value. The error is normalized by the total trace time and then arbitrarily multiplied by 100.

A fraction of traces contain multiple pumping events. For these traces, we assume that the AHA2 dependent leak and the proton-pumping rate are the same for each event. For the vast majority of traces with multiple events this assumption results in good fits to the data (see for example Fig. 3B, C of the main text), however a few percent of traces would be better fit if this condition was relaxed.

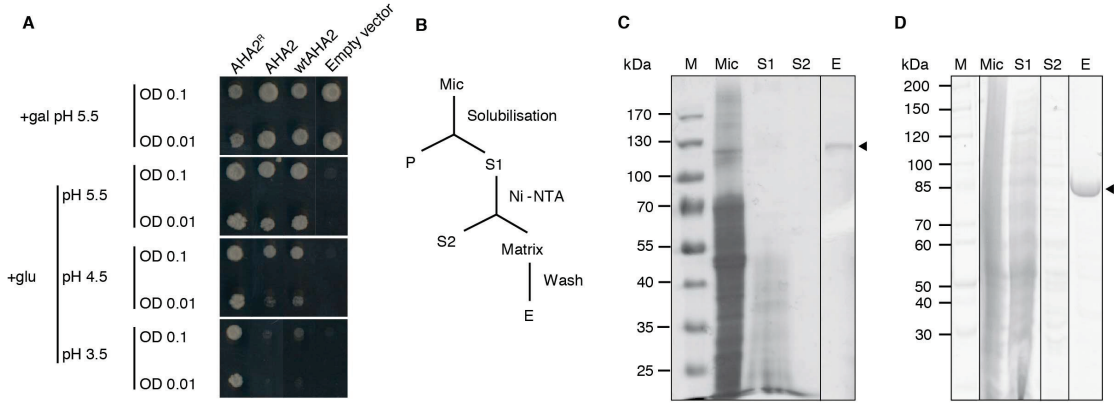

Fig. S1. Expression and purification of H^+-ATPases AHA2 and $AHA2^R$.

(**A**) Regulation of AHA2 activity is not affected by N-terminal His/SNAP tag. A yeast complementation test was performed for non-tagged wild type H^+-ATPase (wtAHA2), AHA2 with a N-terminal His/SNAP tag (AHA2), and C-terminal truncated H^+-ATPase with a C-terminal His tag ($AHA2^R$). An empty vector construct was included as a negative control. In the yeast strain RS-72, the endogenous yeast PM H^+-ATPase, Pma1p, has been placed under the control of a galactose promoter, whereas the introduced, plasmid-borne plant PM H^+-ATPases are under the control of the constitutive PMA1 promoter. Yeast growth on glucose is therefore dependent on a functional plasmid-borne H^+-ATPase. Transformed yeast cells, were spotted on either galactose-containing media (+gal) at pH 5.5 or glucose-containing media (+glu) at different pH values at two different concentrations (OD_{600} = 0.1 and OD_{600} = 0.01). Growth was recorded after 4 days at 30°C. Both wtAHA2 and AHA2 were unable to support growth at pH 3.5, whereas the activated truncated $AHA2^R$ supported growth at all pH values. (**B**) Schematic illustration of the purification steps utilizing classical Ni^{2+}-affinity batch-binding procedure. (**C, D**) Coomassie Brilliant Blue-stained SDS-PAGE on fractions from each purification step illustrating the progressive purification of AHA2 (**C**) and $AHA2^R$ (**D**). Molecular mass markers (M) are indicated on the left. Abbreviations: Mic, microsomes; P, pellet; S1-S4, supernatant 1-4; Mat, matrix after elution; E, concentrated eluate. Specific ATPase activity of DDM solubilized $AHA2^R$ and AHA2 were measured as 15 ± 5 µmol Pi/min/mg of protein (n=7) and 16 ± 8 µmol Pi/min/mg of protein (n=5), respectively.

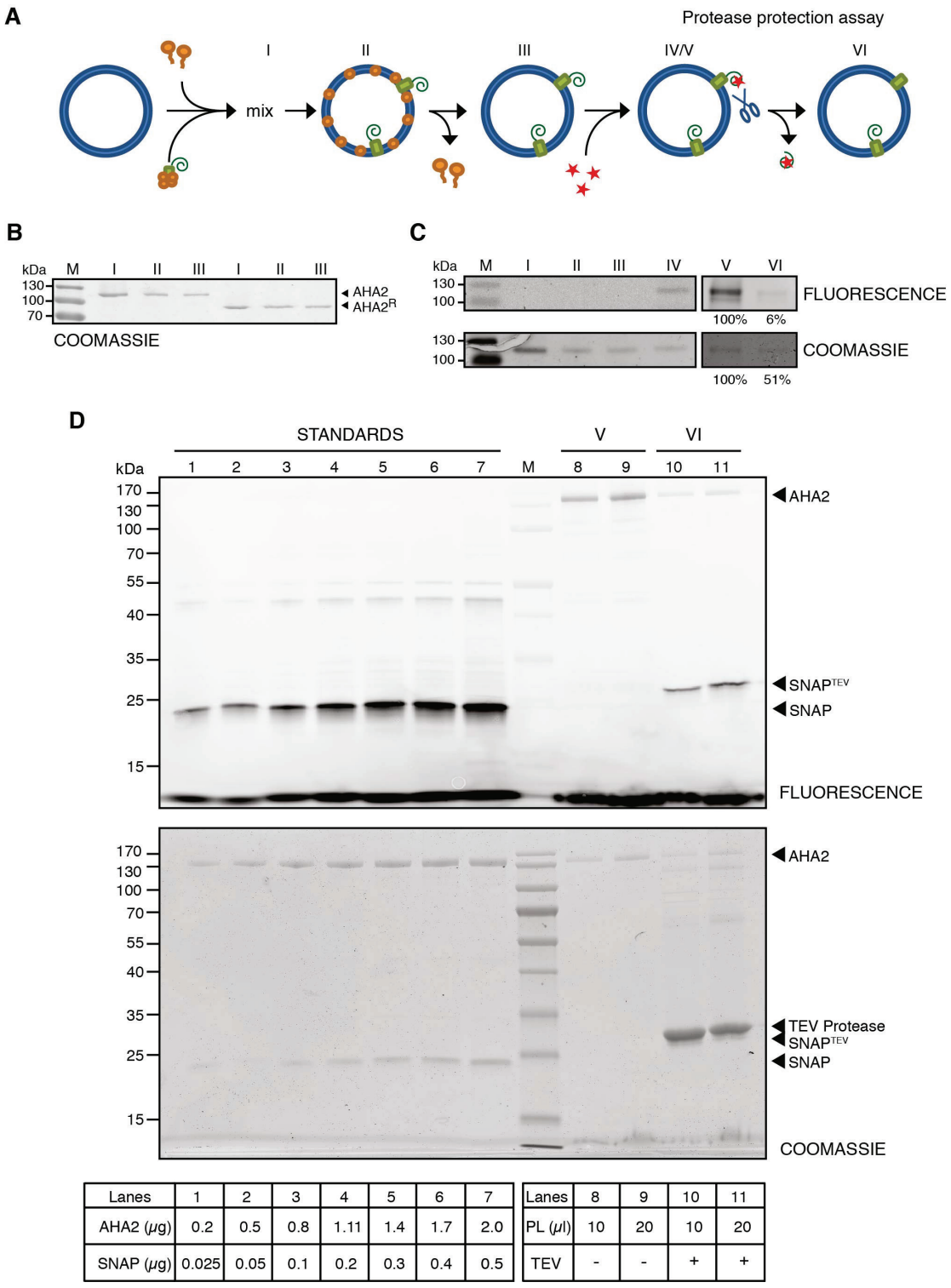

Lanes	1	2	3	4	5	6	7
AHA2 (μg)	0.2	0.5	0.8	1.11	1.4	1.7	2.0
SNAP (μg)	0.025	0.05	0.1	0.2	0.3	0.4	0.5

Lanes	8	9	10	11
PL (μl)	10	20	10	20
TEV	-	-	+	+

Fig. S2. Reconstitution of H^+-ATPases AHA2 and $AHA2^R$. Fluorescence labeling and orientation of reconstituted AHA2.

(**A**) Schematic diagram illustrating the reconstitution, fluorescence labelling, and membrane orientation of AHA2 (endowed with a SNAP coding sequence and a MRGSH6 tag at the N-terminus). Preformed liposomes containing trace amounts of lipid-

linked pHrodo sensor are detergent-destabilized and mixed with the detergent-solubilized pump. Subsequent removal of the detergent by Sephadex G-50 gel filtration and Bio-Bead treatment result in the formation of sealed proteoliposomes. The resulting proteoliposomes were labelled according to manufacturer's instructions using a 2-fold excess of SNAP-Surface® Alexa Fluor® 647 fluorescent substrate compared to AHA2. AHA2 orientation in the proteoliposomes and the degree of labelling was estimated from proteolytic assays using trypsin or Tobacco Etch Virus (TEV) proteases, respectively. Roman numerals refer to samples applied to the corresponding lanes in panel B, C, and D. (**B**) Coomassie Brilliant Blue -stained SDS-PAGE on samples collected at reconstitution steps I-III for $AHA2^R$ and AHA2, demonstrating successful reconstitution of the protein. (**C**) Fluorescent scan (FLUORESCENCE) and corresponding Coomassie Brilliant Blue stained SDS-PAGE (COOMASSIE) on samples collected at reconstitution and labelling steps I-IV, and before and after Trypsin digestion (V,VI). The gels demonstrate successful reconstitution and labelling of AHA2 in proteoliposomes. Numbers under the gel refer to the quantification of the band intensities. As estimated from the analysis on band intensities after trypsin digestion, ~51% of AHA2 in the proteoliposomes was protected from digestion. Efficiency of the digest is demonstrated by almost complete loss of AHA2 fluorescence after trypsin digest. From a total of four independent experiments the orientation of AHA2 was determined to be 80±19% outwards directed AHA2. (**D**) Representative fluorescent scan (FLUORESCENCE) and corresponding Coomassie Brilliant Blue stained SDS-PAGE (COOMASSIE) from the TEV protease assay. Lanes 1-7 contain known amounts of AHA2 and SNAP-tag® Purified Protein (SNAP) prelabelled with SNAP-Surface® Alexa Fluor® 647. Lanes 8, 9: 10 and 20 µl of AHA2 containing proteoliposomes labelled with a 2-fold excess of SNAP-Surface® Alexa Fluor® 647, respectively. Lanes 10, 11: 10 and 20 µl of AHA2 containing proteoliposomes labelled with a 2-fold excess of SNAP-Surface® Alexa Fluor® 647 and digested using TEV protease. The SNAP tag cleaved off from AHA2 is denoted $SNAP^{TEV}$. Molecular mass markers (M) are shown on the left. Based on the protein standards of AHA2 and labeled SNAP the amount of total AHA2 (lane 8, 9) and labeled AHA2 (lane 10, 11) was estimated, and the degree of labeling was calculated to be in the range of 53 ± 12% (n=3, SD). Band intensities were quantified using either the GelQuant.NET software provided by biochemlabsolutions.com or Image Lab™ Software from Bio-Rad.

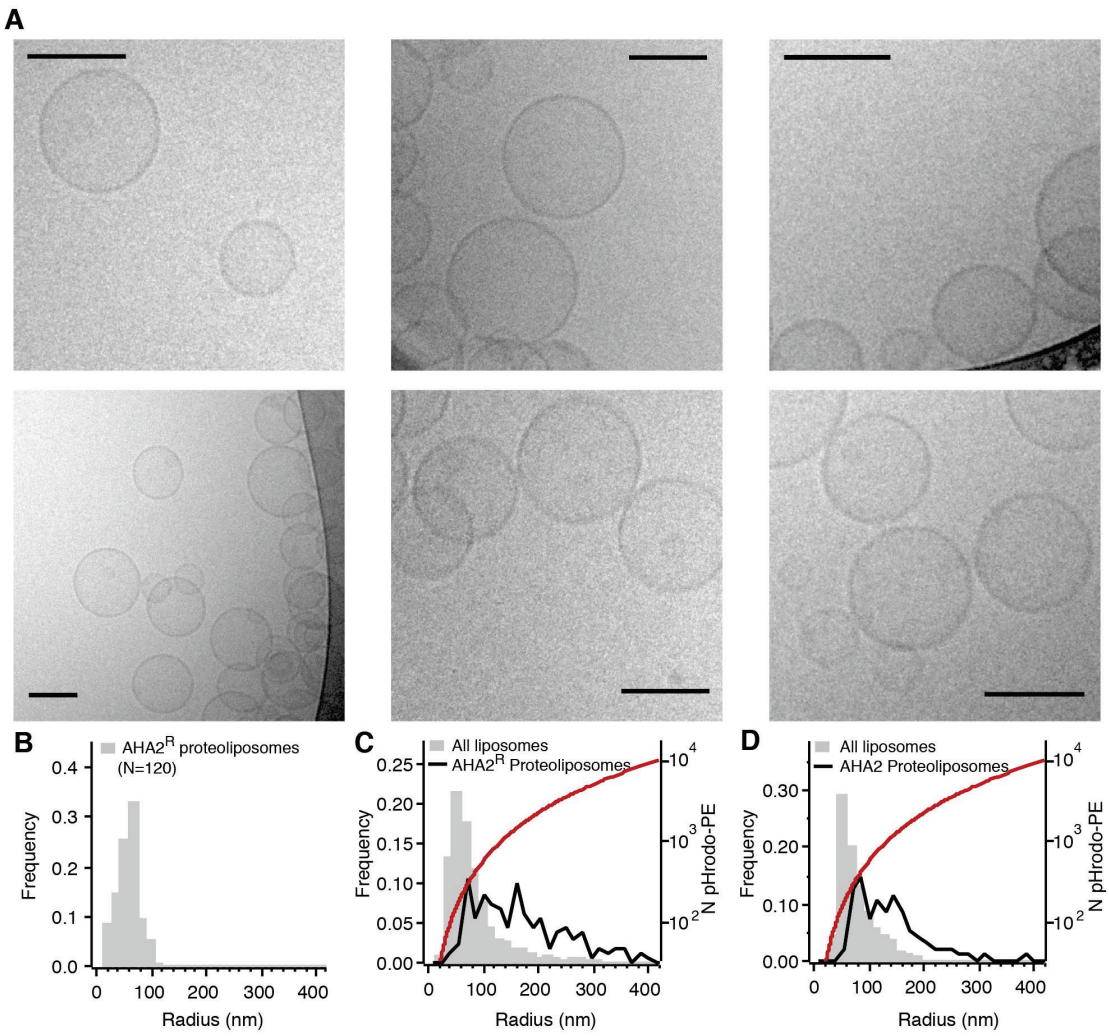

Fig. S3. Cryogenic transmission electron microscopy and size calibration of vesicles. (**A**) Representative micrographs of AHA2^R reconstituted vesicles. The proteoliposomes are highly unilamellar and spherical. All scale bars are 100 nm. (**B**) Size distribution of AHA2^R reconstituted vesicles as measured by cryoTEM. The histogram is fitted with a Gaussian function with a mean value of 51 ± 1.5 nm. (**C**) and (**D**) show the size distributions of AHA2^R and AHA2 reconstituted vesicles respectively, as determined by TIRF microscopy. Because the microscope settings were optimized to minimize bleaching, vesicles smaller than ~60 nm in diameter were not detected. Size histograms of all detected liposomes are shown in grey, while size histograms of proteoliposomes that showed lumen acidification are shown in black. Notice that due to low protein/lipid ratio only the larger vesicles contain active proton pumps. Red lines represent the estimated number of pHrodo-PE molecules for liposomes of different sizes, which for active liposomes are 350-10,000. First surface area of the liposomes with given radius was calculated. Number of lipid molecules for different size vesicles was then estimated using a surface area per lipid of 0.7 nm^2 and the thickness of bilayer 3.63 nm (*45-47*).

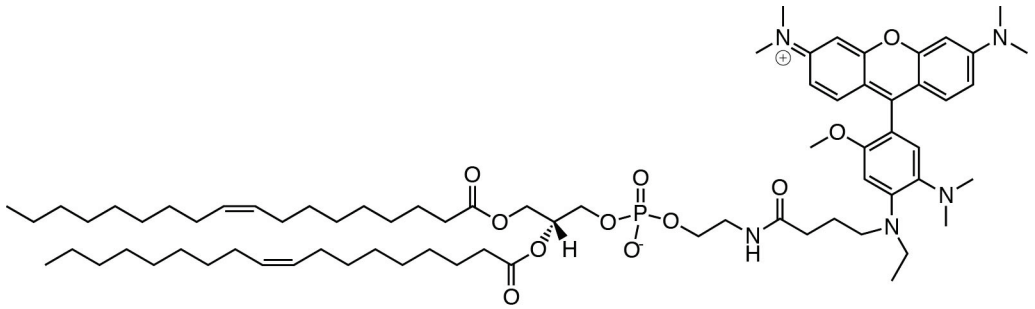

Fig. S4. Chemical structure of the lipid conjugated pH-sensor PE-pHrodo.
For a detailed description of purification and characterization of PE-pHrodo please see reference (*16*).

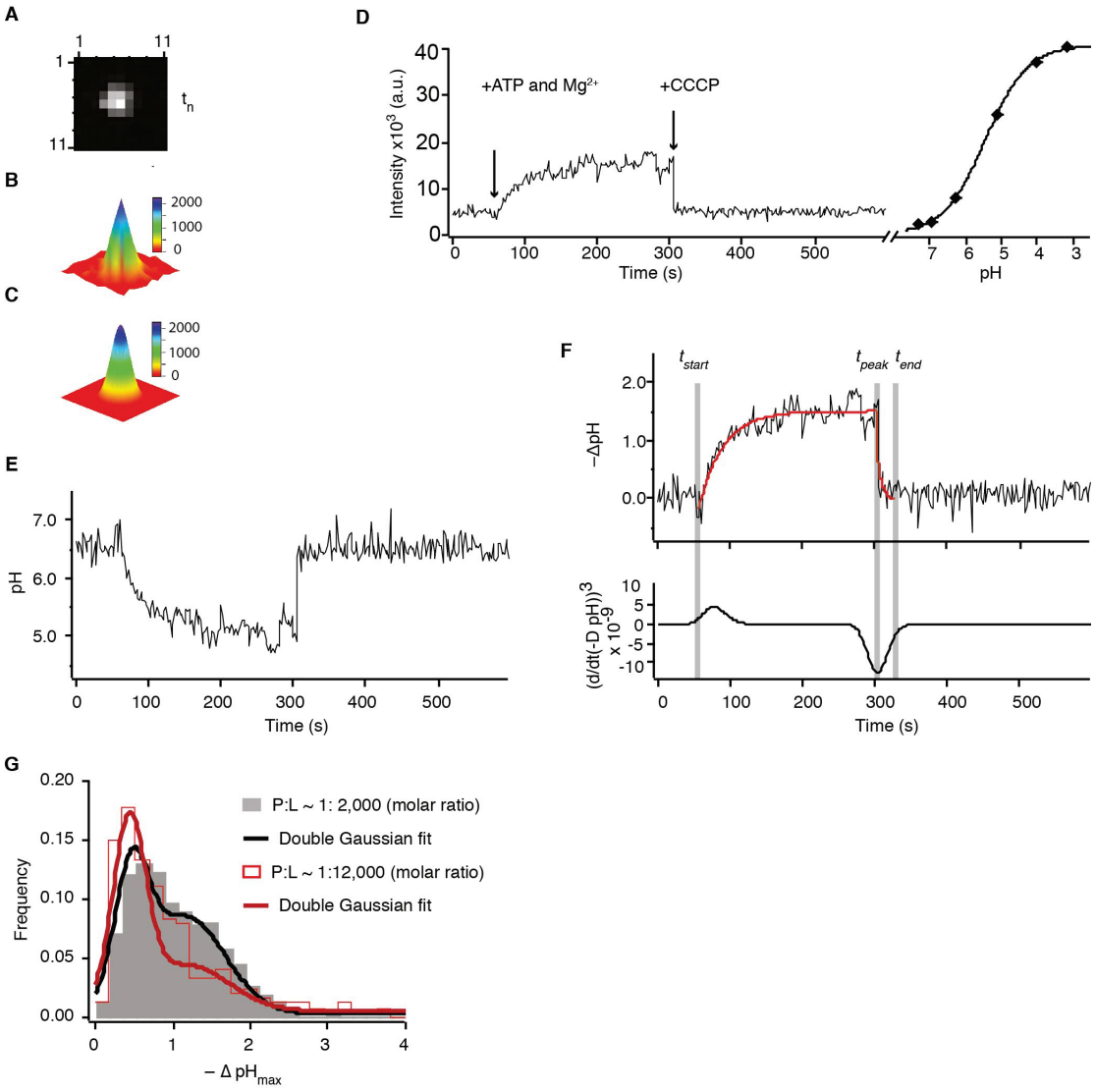

Fig. S5. Extracting single-vesicle intensities from fluorescence microscopy images and calibrating them in pH units.

(**A**) 11x11 pixel region of interest (ROI) cropped from a typical micrograph and centred around a surface tethered proteoliposome. (**B**) 3D representation of the intensity values in (a). (**C**) 2D Gaussian fit of the proteoliposomes in **A**). (**D**) Activity trace of a typical AHA2^{R} – reconstituted proteoliposome and its corresponding pH calibration curve. Proton transport is triggered by addition of ATP and Mg^{2+}, each to a final concentration of 2 mM (t = 60 s). After 300 s, the proton gradient is collapsed by addition of 5 µM CCCP. An activity recording is always followed by the exchange of transport buffer with citrate–phosphate buffers of varying pH (7.3–3) in presence of 60 nM valinomycin to acquire a local pH calibration curve for each proteoliposome. Half of the average baseline intensity is subtracted from the absolute intensity values from (**B**) to account for the non-specific intensity contribution from pHrodo located in the outer monolayer of the proteoliposomes. The baseline is defined by the intensity values recorded before injection of Mg^{2+} and ATP. The intensity values acquired during pH-titration are divided by 2 to

account for the signal coming from the outer monolayer. Subsequently, the pH calibration curve is fitted with a sigmoidal function, which is used to convert the absolute intensity values into pH units. (**E**) The single $AHA2^R$ activity trace from (**D**) converted into pH units. (**F**) The pH gradient generated by the single $AHA2^R$ transporter from (**D**) and (**E**). The corresponding differentiated trace was used to determine t_{start}, t_{peak} and t_{end} for the single transporter event, as indicated by the grey bars. The red trace show exponential functions fitted to the data. (**G**) Population histogram of pH plateaus for $AHA2^R$ at different protein-to-lipid ratios demonstrating that the binomial distribution of plateaus is modulated by changes in the P:L ratio and thus reflects the number of single molecules. For the grey and red traces respectively: number of independent experiments was 2 and 3; number of individual proteoliposomes analysed was 425 and 167; number of events counted was 427 and 241. Note: Red histogram here is the same as (B) in main Figure 2.

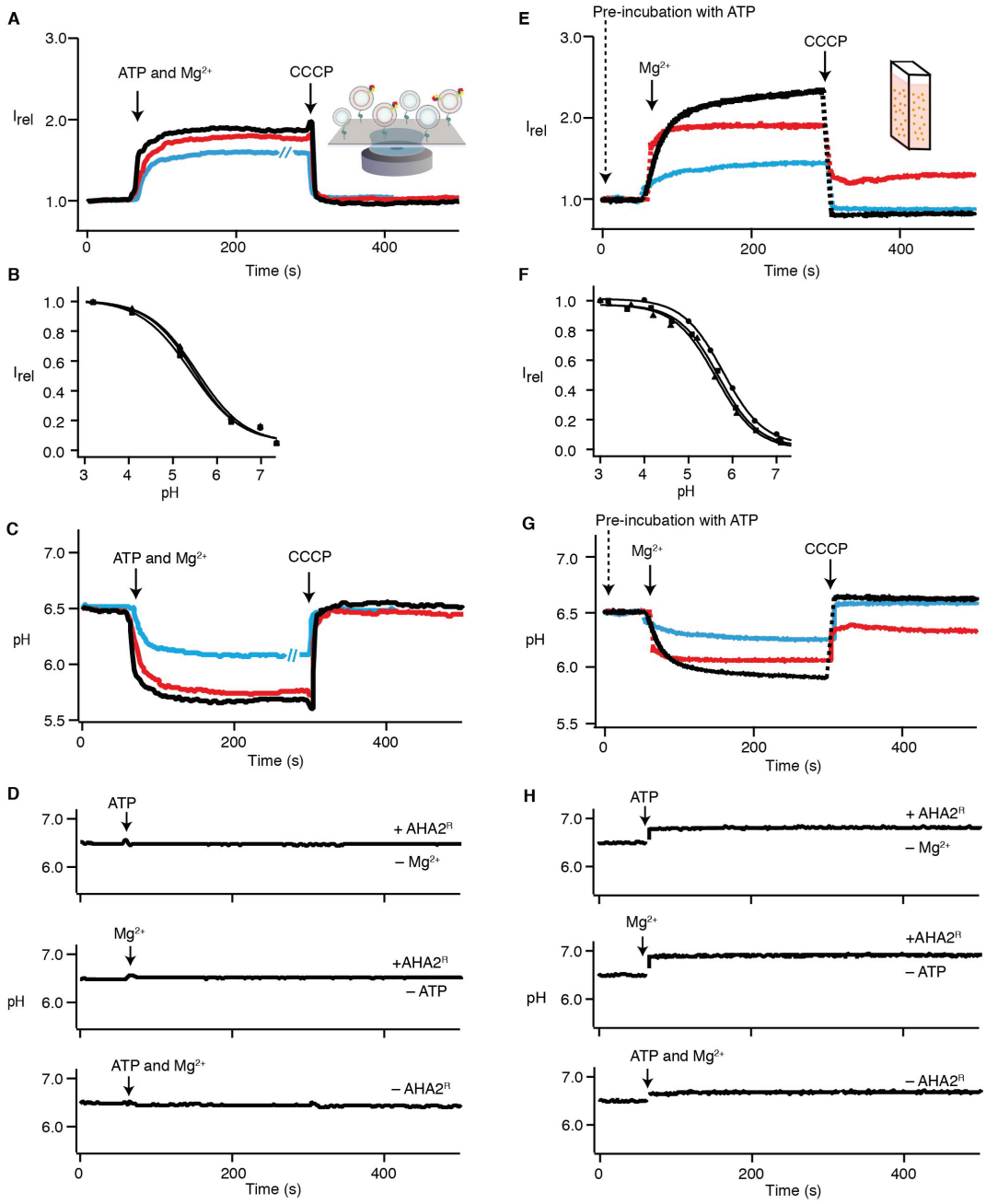

Fig. S6. Proton pumping by AHA2^{R}: single vesicle and macroscopic ensemble-average experiments compare well within experimental uncertainties.

(**A–D**) Three typical single vesicles experiments recorded with fluorescence microscopy. (**E–H**) Three typical ensemble average experiments recorded with spectrophotometer. (**A & E**) Evolution of fluorescence intensity upon addition of ATP, Mg^{2+} and CCCP as indicated. (**B & F**) pH calibration curves obtained from single vesicle experiments and macroscopic ensemble-average experiment. Different symbols denote data from independent experiments; lines represent sigmoidal fits to the data. (**C & G**) Fluorescent activity traces from (**A**) and (**E**) converted to pH units. (**D & H**) Control experiments carried out in absence of ATP and/or Mg^{2+} (t = 60 s) for AHA2^{R}-reconstituted liposomes

for both single vesicles (**D**) and ensemble-average experiment (**H**). The last trace for the panel **(D**) and (**H**) represents absence of any activity upon addition of ATP and Mg^{2+} to mock liposomes, i.e. liposomes without $AHA2^{R}$**.**

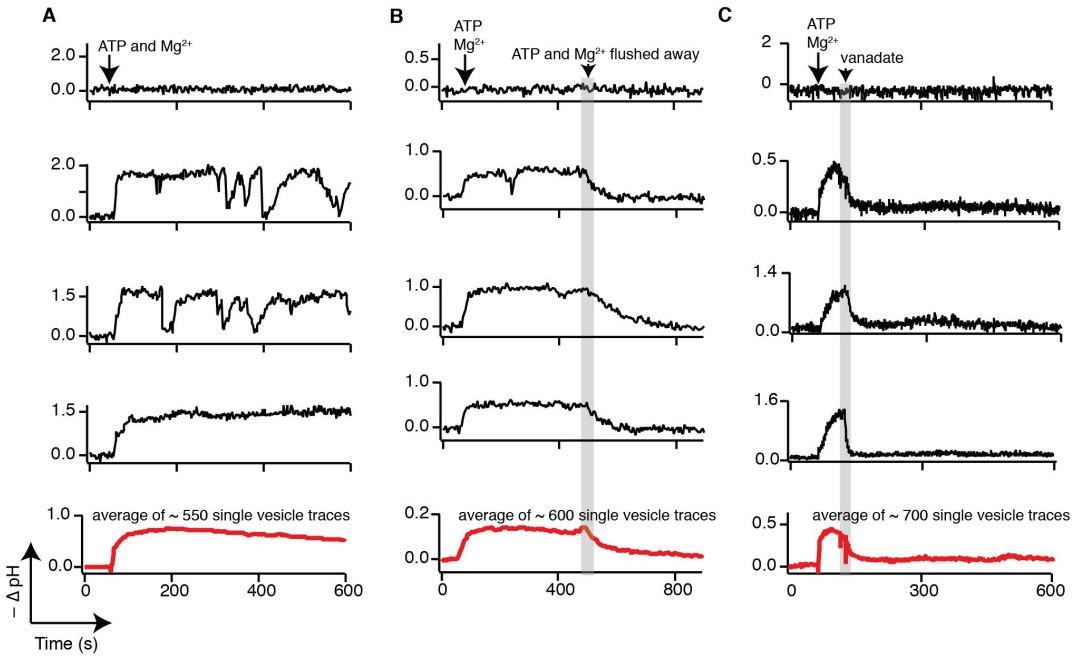

Fig. S7. Additional controls for specific proton pumping activity.

Activity of AHA^R-reconstituted proteoliposomes under different conditions. (**A-C**) Single vesicle traces (black) and ensemble-average of single vesicle particles (red trace) for activity assays carried out under different conditions. Traces on the top panel represent inactive or empty vesicles. (**A**) Activity assays were performed under constant flow of ATP and Mg^{2+} (2 mM in transport buffer) to ensure that pH fluctuations were not due to ATP depletion. (**B**) To further confirm that proton pumping was specific to the addition of energy in the form of ATP, ATP and Mg^{2+} were flushed away during the activity assay (t = 500 s, grey line). As expected, a decline in the established pH gradient was observed. The kinetics were limited by the time it took to exchange fully buffers. (**C**) Proton pumping was triggered at 60 s with the addition of ATP and Mg^{2+}, and subsequently inhibited by the addition of the specific blocker vanadate at t =120 s (grey line).

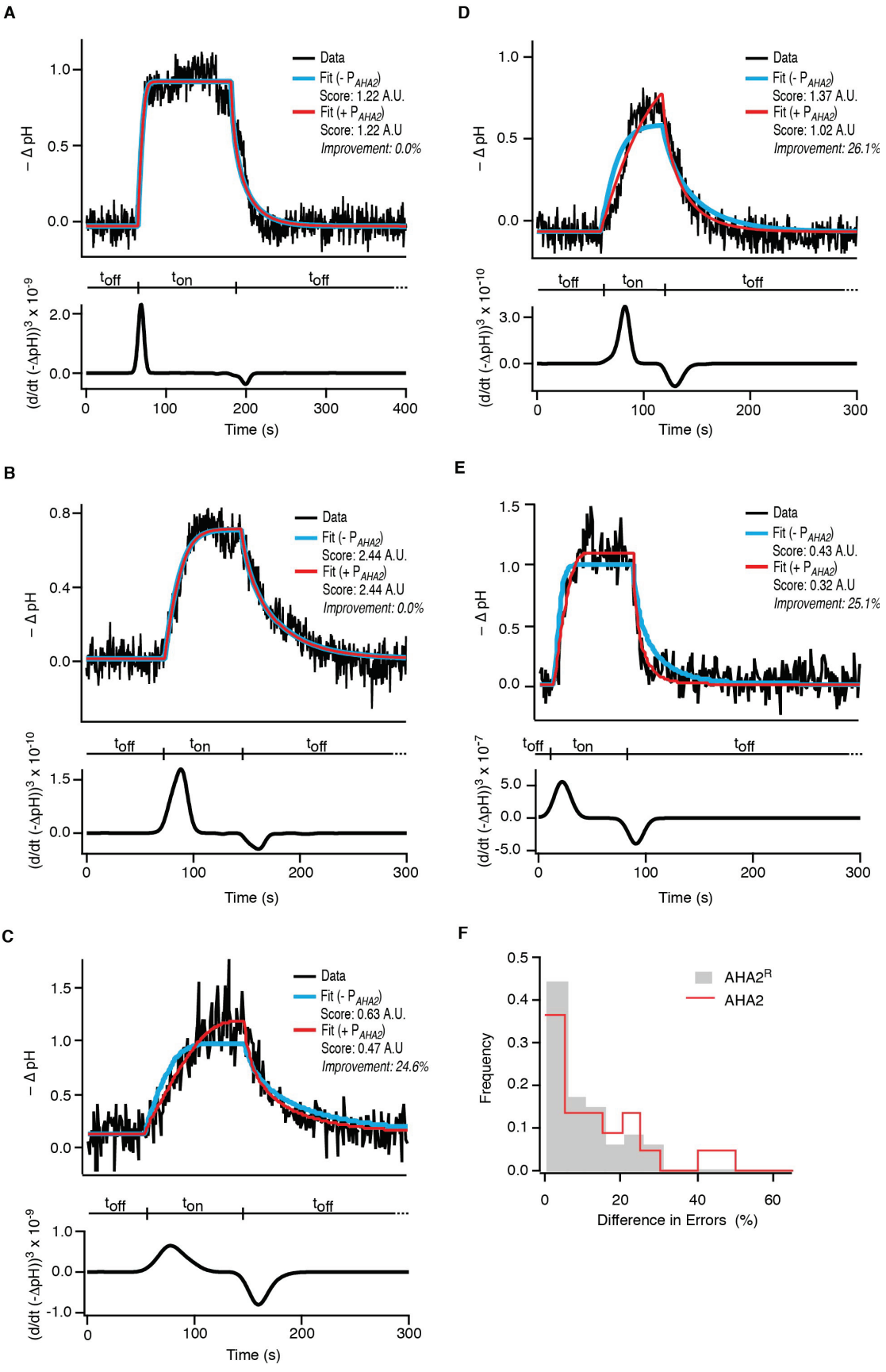
A
Data
Fit (- P_AHA2)
Score: 1.22 A.U.
Fit (+ P_AHA2)
Score: 1.22 A.U
Improvement: 0.0%
– Δ pH
toff
ton
toff
(d/dt (-ΔpH))3 x 10-9
Time (s)
D
Data
Fit (- P_AHA2)
Score: 1.37 A.U.
Fit (+ P_AHA2)
Score: 1.02 A.U
Improvement: 26.1%
– Δ pH
(d/dt (-ΔpH))3 x 10-10
Time (s)
B
Data
Fit (- P_AHA2)
Score: 2.44 A.U.
Fit (+ P_AHA2)
Score: 2.44 A.U
Improvement: 0.0%
– Δ pH
(d/dt (-ΔpH))3 x 10-10
Time (s)
E
Data
Fit (- P_AHA2)
Score: 0.43 A.U.
Fit (+ P_AHA2)
Score: 0.32 A.U
Improvement: 25.1%
– Δ pH
(d/dt (-ΔpH))3 x 10-7
Time (s)
C
Data
Fit (- P_AHA2)
Score: 0.63 A.U.
Fit (+ P_AHA2)
Score: 0.47 A.U
Improvement: 24.6%
– Δ pH
(d/dt (-ΔpH))3 x 10-9
Time (s)
F
AHA2R
AHA2
Frequency
Difference in Errors (%)

Fig. S8. Typical single molecule proton pumping kinetics fitted with the model.

(**A-E**) Raw traces from single vesicle kinetics fitted with a physical model in the absence (-P_{AHA2}, blue fits) or presence (+P_{AHA2}, red fits) respectively of a time-dependent proton leakage associated with the protein. Zoom into the areas of activity. The corresponding first derivative of the kinetics was used to determine when the proton pump spend in an acitive (t_{on}) or inactive state (t_{off}). Traces (**A-B**) were successfully fitted both by the simplest model while traces (**C-E**) required a passive leak (P_{AHA2}) starting as soon as pumping is switched off in order to fit well both the rise, the decline and the plateau of the traces. (**F**) Histogram of percentage improvement in the fitting errors for the traces where P_{AHA2} was included for AHA2 and AHA2^{R} traces. The errors are dominated by the typically larger portion of the trace that is at background/zero, where the two fits are naturally overlapping. For that reason the global relative improvement is typically < 20%.

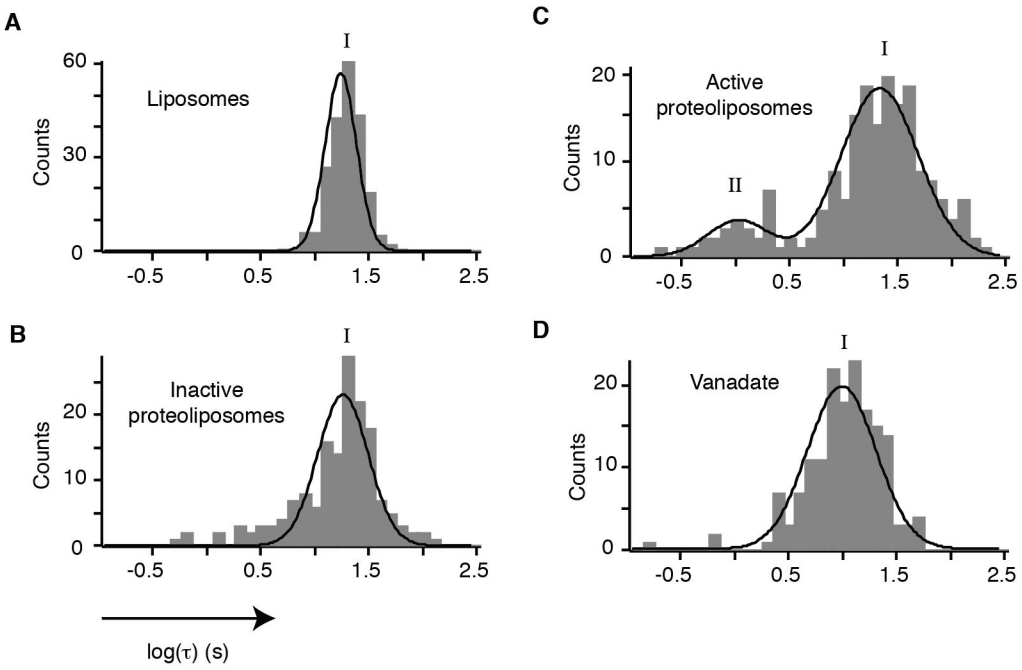

Fig. S9. Histograms of proton leakage lifetimes under various conditions.

(**A–D**) Histograms of leakage lifetimes for (**A**) liposomes, (**B**) inactive proteoliposomes, (**C**) active proteoliposomes and (**D**) active proteoliposomes in presence of 500 μM vanadate. The lifetimes for (**A**) and (**B**) were derived from passive leakage experiments described in fig. S10, while for (**C**) and (**D**), they were obtained from pH decays in activity traces (see Figure 2 in main text, and Supplementary Fig. 7, 8). Histograms were fitted to single (**A**, **B**, and **D**) and double (**C**) Gaussian distributions. Note: In a typical activity assay, i.e. for active proteoliposomes, the pH of the buffer in the bulk is constant (pH=6.5) over the course of the reaction. Therefore, peak II in the histogram for active proteoliposomes is not due to outer monolayer quenching (*cf* fig. S10). Additionally, peak II is absent for proteoliposomes inhibited by vanadate, which further emphasizes the role of $AHA2^R$ in proton leakage.

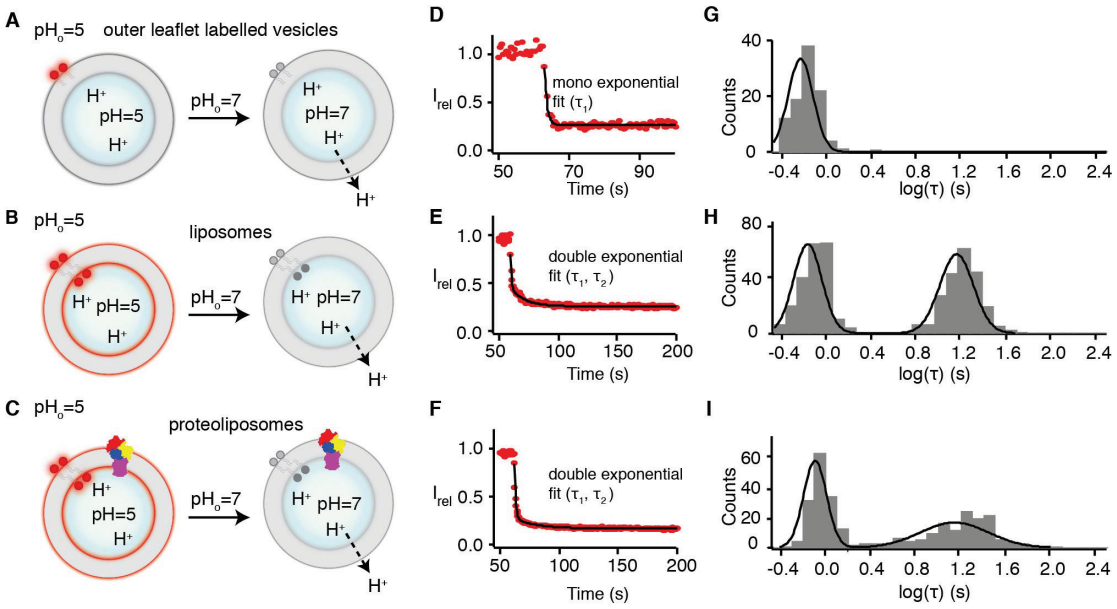

Fig. S10. Method to measure passive proton leakage in single vesicles.

(**A-C**) Schematic representation of leakage test for outer leaflet labelled vesicles (**A**), liposomes subjected to a mock reconstitution procedure identical to proteoliposomes (**B**), and proteoliposomes (**C**). Initially pH_o = pH =5 and the fluorescence intensity from the vesicles is high. We then exchange the external buffer so that pH_o=7, and follow the kinetics of signal decrease. (**D-F**) Illustrative kinetics of fluorescence decrease upon buffer exchange for three typical single vesicles, respectively from samples a-c. Each individual fluorescent trace was fitted to a mono exponential for outer leaflet labelled vesicles (**D**) and double exponential decay fit for liposomes (**E**) and proteoliposomes (**F**) to obtain both fast (τ_1) and slow (τ_2) leakage life times. T-test of the residuals was used to obtain the best-fit model. (**G**) Histograms of leakage lifetimes (τ_1) derived from fluorescent traces of single vesicles fitted to single Gaussian to yield an average lifetime of 0.67 ± 0.09 s. (**H-I**) Histograms of leakage lifetimes (τ_1 and τ_2) derived from fluorescent traces of single vesicles fitted to a double Gaussian. The average lifetime (τ_1) was 0.77 ± 0.16 s for liposomes and 0.81 ± 0.15 s for proteoliposomes. Such small shifts in the maxima of the distributions occurred between reconstitutions. The leakage rate was always constant over the time, i.e., no abrupt changes in the leakage rate or any sort of stalling was ever observed.

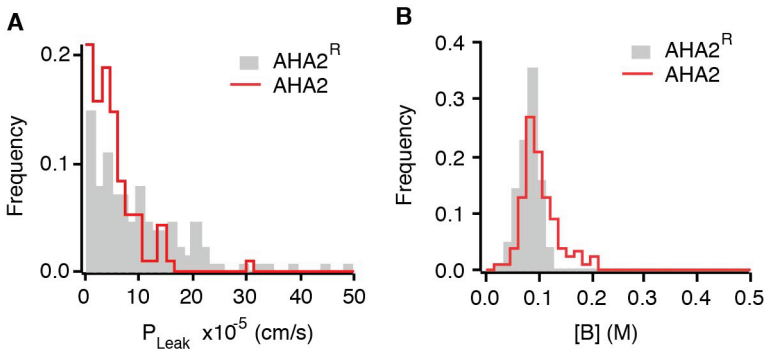

Fig. S11. Histograms of additional physical parameters quantified by the model.
(A) Membrane permeability distributions (P_{Leak}) for AHA2 and AHA2^R. (B) Distribution of membrane impermeable negative charges for AHA2 and AHA2^R proteoliposomes.

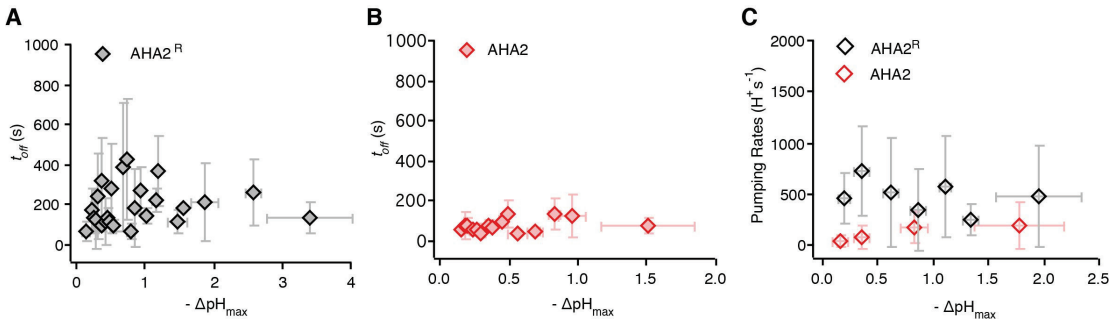

Fig. S12. Established pH gradients have no significant effect on off times and pumping rates of AHA2^R and AHA2.

(**A**, **B**) Relation between t_{off} and the maximal pH gradient for AHA2^R and AHA2 respectively. Each data point represents the average of 3 consecutive values. (**C**) Pumping rates as a function of established pH gradient. Data were binned with 0.25 and 0.5 pH units. For AHA2^R and AHA2 respectively: number of independent experiments was 3 and 2, while number of analysed individual proteoliposomes was 126 and 95. Error bars represent standard deviations.

Table S1.

ATP permeability of proteoliposomes

t (min)	γ-counts[1] (cpm)	F[2] (A.U.)	Rel. γ-counts[3]	ATP recovery[4]
1	4193	1.04E+06	4.04E-03	100%
30	3800	9.50E+05	4.00E-03	99%
60	3997	1.00E+06	3.99E-03	99%
120	3998	1.05E+06	3.82E-03	95%

[1]γ-counts, radioactivity in counts per minute; [2]F, recovery of proteoliposomes based on Rhodamine-PE fluorescence intensity; [3]Relative γ-counts, calculated by dividing γ-counts by F; [4]ATP recovery, normalized relative γ-counts to the value at 1 min.

Table S2.

Model parameters.

Variable name	symbol	value	units
Extracellular potassium concentration	$[K]_0^+$	105	mM
Intracellular potassium concentration (initial)	$[K]^+$	see text	mM
Extracellular pH value	pH_0	6.5	
Intracellular pH value (initial)	pH(0)	see text	
Intracellular total protons (initial)	H^+	see text	number
Buffer total concentration	T^1	10	mM
Dye molecule total concentration	T^2	2.5	mM
Buffer log diss. constant	pK_a^1	6.15	
Dye molecule log diss. constant (wild type AHA2)	pK_a^2	5.72	
Dye molecule log diss. constant (truncated AHA2)	pK_a^2	5.82	
Potassium permeability	P_K	10^{-7}	cm/s
Vesicle radius	R	experiment & equation 1	nm
Constant in Eq. 1 ($AHA2^R$ data)	k	1.27	
Constant in Eq. 1 (AHA2 data)	k	1.35	
Bilayer capacitance	C_0	1	□F/cm^2
Donnan particles	B	see text	mM
Background proton permeability	P_{leak}	Fit to data	cm/s
AHA2-dependent proton leak	q	Fit to data	cm^3/s
AHA2 pump rate	I_P	Fit to data	# ions/s

REFERENCES AND NOTES

1. F. Ashcroft, D. Gadsby, C. Miller, Introduction. The blurred boundary between channels and transporters. *Philos. Trans. R. Soc. London Ser. B* **364**, 145–147 (2009). Medline doi:10.1098/rstb.2008.0245

2. E. Neher, B. Sakmann, Single-channel currents recorded from membrane of denervated frog muscle fibres. *Nature* **260**, 799–802 (1976). Medline doi:10.1038/260799a0

3. J. P. Morth, B. P. Pedersen, M. J. Buch-Pedersen, J. P. Andersen, B. Vilsen, M. G. Palmgren, P. Nissen, A structural overview of the plasma membrane Na^+,K^+-ATPase and H^+-ATPase ion pumps. *Nat. Rev. Mol. Cell Biol.* **12**, 60–70 (2011). Medline doi:10.1038/nrm3031

4. L. J. DeFelice, T. Goswami, Transporters as channels. *Annu. Rev. Physiol.* **69**, 87–112 (2007). Medline doi:10.1146/annurev.physiol.69.031905.164816

5. R. Peters, Optical single transporter recording: Transport kinetics in microarrays of membrane patches. *Annu. Rev. Biophys. Biomol. Struct.* **32**, 47–67 (2003). Medline doi:10.1146/annurev.biophys.32.110601.142429

6. A. Tonnesen, S. M. Christensen, V. Tkach, D. Stamou, Geometrical membrane curvature as an allosteric regulator of membrane protein structure and function. *Biophys. J.* **106**, 201–209 (2014). Medline doi:10.1016/j.bpj.2013.11.023

7. R. Watanabe, N. Soga, D. Fujita, K. V. Tabata, L. Yamauchi, S. Hyeon Kim, D. Asanuma, M. Kamiya, Y. Urano, H. Suga, H. Noji, Arrayed lipid bilayer chambers allow single-molecule analysis of membrane transporter activity. *Nat. Commun.* **5**, 4519 (2014). Medline doi:10.1038/ncomms5519

8. M. Li, S. K. Jørgensen, D. G. McMillan, Ł. Krzemiński, N. N. Daskalakis, R. H. Partanen, M. Tutkus, R. Tuma, D. Stamou, N. S. Hatzakis, L. J. Jeuken, Single enzyme experiments reveal a long-lifetime proton leak state in a heme-copper oxidase. *J. Am. Chem. Soc.* **137**, 16055–16063 (2015). Medline

9. B. P. Pedersen, M. J. Buch-Pedersen, J. P. Morth, M. G. Palmgren, P. Nissen, Crystal structure of the plasma membrane proton pump. *Nature* **450**, 1111–1114 (2007). Medline doi:10.1038/nature06417

10. M. G. Palmgren, C. Larsson, M. Sommarin, Proteolytic activation of the plant plasma membrane H^+-ATPase by removal of a terminal segment. *J. Biol. Chem.* **265**, 13423–13426 (1990). Medline

11. M. G. Palmgren, P. Nissen, P-type ATPases. *Annu. Rev. Biophys.* **40**, 243–266 (2011). Medline doi:10.1146/annurev.biophys.093008.131331

12. See materials and methods and supplementary information on *Science* Online

13. S. Mathiasen, S. M. Christensen, J. J. Fung, S. G. Rasmussen, J. F. Fay, S. K. Jorgensen, S. Veshaguri, D. L. Farrens, M. Kiskowski, B. Kobilka, D. Stamou, Nanoscale high-content analysis using compositional heterogeneities of single proteoliposomes. *Nat. Methods* **11**, 931–934 (2014). Medline doi:10.1038/nmeth.3062

14. P. M. Bendix, M. S. Pedersen, D. Stamou, Quantification of nano-scale intermembrane contact areas by using fluorescence resonance energy transfer. *Proc. Natl. Acad. Sci. U.S.A.* **106**, 12341–12346 (2009). Medline doi:10.1073/pnas.0903052106

15. D. Stamou, C. Duschl, E. Delamarche, H. Vogel, Self-assembled microarrays of attoliter molecular vessels. *Angew. Chem. Int. Ed.Engl.* **42**, 5580–5583 (2003). Medline doi:10.1002/anie.200351866

16. G. C. Kemmer, S. A. Bogh, M. Urban, M. G. Palmgren, T. Vosch, J. Schiller, T. Günther Pomorski, Lipid-conjugated fluorescent pH sensors for monitoring pH changes in reconstituted membrane systems. *Analyst* **140**, 6313–6320 (2015). Medline doi:10.1039/C5AN01180A

17. L. Iversen, H. L. Tu, W. C. Lin, S. M. Christensen, S. M. Abel, J. Iwig, H. J. Wu, J. Gureasko, C. Rhodes, R. S. Petit, S. D. Hansen, P. Thill, C. H. Yu, D. Stamou, A. K. Chakraborty, J. Kuriyan, J. T. Groves, Ras activation by SOS: Allosteric regulation by altered fluctuation dynamics. *Science* **345**, 50–54 (2014). Medline doi:10.1126/science.1250373

18. M. J. Comstock, K. D. Whitley, H. Jia, J. Sokoloski, T. M. Lohman, T. Ha, Y. R. Chemla, Direct observation of structure-function relationship in a nucleic acid-processing enzyme. *Science* **348**, 352–354 (2015). Medline doi:10.1126/science.aaa0130

19. T. Yanagida, Y. Ishii, Eds., *Single Molecule Dynamics in Life Science* (Wiley-VCH, Weinheim, Germany, 2009).

20. X. S. Xie, in *Single Molecule Spectroscopy in Chemistry, Physics and Biology*, A. Graslund, R. Rigler, J. Widengren, Eds. (Springer-Verlag Berlin, 2010), vol. 96, pp. 435–448.

21. N. Akyuz, E. R. Georgieva, Z. Zhou, S. Stolzenberg, M. A. Cuendet, G. Khelashvili *et al.*, Transport domain unlocking sets the uptake rate of an aspartate transporter. *Nature* **518**, 68 (2015).

22. C. E. Aitken, J. D. Puglisi, Following the intersubunit conformation of the ribosome during translation in real time. *Nat. Struct. Mol. Biol.* **17**, 793–800 (2010). Medline doi:10.1038/nsmb.1828

23. G.-W. Li, E. Oh, J. S. Weissman, The anti-Shine-Dalgarno sequence drives translational pausing and codon choice in bacteria. *Nature* **484**, 538–541 (2012). Medline doi:10.1038/nature10965

24. A. R. Subramaniam, B. M. Zid, E. K. O'Shea, An integrated approach reveals regulatory controls on bacterial translation elongation. *Cell* **159**, 1200–1211 (2014). Medline doi:10.1016/j.cell.2014.10.043

25. B. Sakmann, E. Neher, Eds., *Single-Channel Recording* (Springer, New York, ed. 2, 2009).

26. M. Grabe, G. Oster, Regulation of organelle acidity. *J. Gen. Physiol.* **117**, 329–344 (2001). Medline doi:10.1085/jgp.117.4.329

27. M. C. Berman, Slippage and uncoupling in P-type cation pumps; implications for energy transduction mechanisms and regulation of metabolism. *Biochim. Biophys. Acta* **1513**, 95–121 (2001). Medline doi:10.1016/S0005-2736(01)00356-X

28. N. Nelson, A. Sacher, H. Nelson, The significance of molecular slips in transport systems. *Nat. Rev. Mol. Cell Biol.* **3**, 876–881 (2002). Medline doi:10.1038/nrm955

29. M. G. Palmgren, M. Sommarin, R. Serrano, C. Larsson, Identification of an autoinhibitory domain in the C-terminal region of the plant plasma membrane H^+-ATPase. *J. Biol. Chem.* **266**, 20470–20475 (1991). Medline

30. F. C. Lanfermeijer, K. Venema, M. G. Palmgren, Purification of a histidine-tagged plant plasma membrane H^+-ATPase expressed in yeast. *Protein Expr. Purif.* **12**, 29–37 (1998). Medline doi:10.1006/prep.1997.0788

31. J. E. Hill, A. M. Myers, T. J. Koerner, A. Tzagoloff, Yeast/*E. coli* shuttle vectors with multiple unique restriction sites. *Yeast* **2**, 163–167 (1986). Medline doi:10.1002/yea.320020304

32. A. Cid, R. Perona, R. Serrano, Replacement of the promoter of the yeast plasma membrane ATPase gene by a galactose-dependent promoter and its physiological consequences. *Curr. Genet.* **12**, 105–110 (1987). Medline doi:10.1007/BF00434664

33. B. Regenberg, J. M. Villalba, F. C. Lanfermeijer, M. G. Palmgren, C-terminal deletion analysis of plant plasma membrane H^+-ATPase: Yeast as a model system for solute transport across the plant plasma membrane. *Plant Cell* **7**, 1655–1666 (1995). Medline

34. W. Liang, T. Levchenko, B. A. Khaw, V. Torchilin, ATP-containing immunoliposomes specific for cardiac myosin. *Curr. Drug Deliv.* **1**, 1–7 (2004). Medline doi:10.2174/1567201043480063

35. K. Ekberg, M. G. Palmgren, B. Veierskov, M. J. Buch-Pedersen, A novel mechanism of P-type ATPase autoinhibition involving both termini of the protein. *J. Biol. Chem.* **285**, 7344–7350 (2010). Medline doi:10.1074/jbc.M109.096123

36. K. Ekberg, A. G. Wielandt, M. J. Buch-Pedersen, M. G. Palmgren, A conserved asparagine in a P-type proton pump is required for efficient gating of protons. *J. Biol. Chem.* **288**, 9610–9618 (2013). Medline doi:10.1074/jbc.M112.417345

37. B. H. Justesen, R. W. Hansen, H. J. Martens, L. Theorin, M. G. Palmgren, K. L. Martinez, T. G. Pomorski, A. T. Fuglsang, Active plasma membrane P-type H^+-ATPase reconstituted into nanodiscs is a monomer. *J. Biol. Chem.* **288**, 26419–26429 (2013). Medline doi:10.1074/jbc.M112.446948

38. M. J. Buch-Pedersen, M. G. Palmgren, Conserved Asp684 in transmembrane segment M6 of the plant plasma membrane P-type proton pump AHA2 is a molecular determinant of proton translocation. *J. Biol. Chem.* **278**, 17845–17851 (2003). Medline doi:10.1074/jbc.M212729200

39. M. Stratton, I. H. Lee, M. Bhattacharyya, S. M. Christensen, L. H. Chao, H. Schulman, J. T. Groves, J. Kuriyan, Correction: Activation-triggered subunit exchange between CaMKII holoenzymes facilitates the spread of kinase activity. *eLife* **3**, e02490 (2014). Medline

40. A. H. Kunding, M. W. Mortensen, S. M. Christensen, D. Stamou, A fluorescence-based technique to construct size distributions from single-object measurements: Application to the extrusion of lipid vesicles. *Biophys. J.* **95**, 1176–1188 (2008). Medline doi:10.1529/biophysj.108.128819

41. D. L. Ensign, V. S. Pande, Bayesian single-exponential kinetics in single-molecule experiments and simulations. *J. Phys. Chem. B* **113**, 12410–12423 (2009). Medline doi:10.1021/jp903107c

42. Y. Ishida, S. Nayak, J. A. Mindell, M. Grabe, A model of lysosomal pH regulation. *J. Gen. Physiol.* **141**, 705–720 (2013). Medline doi:10.1085/jgp.201210930

43. S. L. Rybak, F. Lanni, R. F. Murphy, Theoretical considerations on the role of membrane potential in the regulation of endosomal pH. *Biophys. J.* **73**, 674–687 (1997). Medline doi:10.1016/S0006-3495(97)78102-5

44. W. F. Boron, Regulation of intracellular pH. *Adv. Physiol. Educ.* **28**, 160–179 (2004). Medline doi:10.1152/advan.00045.2004

45. G. Gramlich, J. Zhang, M. Winterhalter, W. M. Nau, A long-lived amphiphilic fluorescent probe studied in POPC air-water monolayer and solution bilayer systems. *Chem. Phys. Lipids* **113**, 1–9 (2001). Medline doi:10.1016/S0009-3084(01)00133-5

46. Y. Tahara, Y. Fujiyoshi, A new method to measure bilayer thickness: Cryo-electron microscopy of frozen hydrated liposomes and image simulation. *Micron* **25**, 141–149 (1994). Medline doi:10.1016/0968-4328(94)90039-6

47. G. Ghale, A. G. Lanctôt, H. T. Kreissl, M. H. Jacob, H. Weingart, M. Winterhalter, W. M. Nau, Chemosensing ensembles for monitoring biomembrane transport in real time. *Angew. Chem. Int. Ed. Engl.* **53**, 2762–2765 (2014). Medline doi:10.1002/anie.201309583